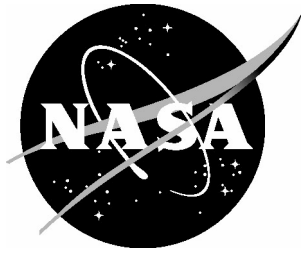


NASA/TM-2005-213781



Turbulent Vortex-Flow Simulation Over a 65° Sharp and Blunt Leading-Edge Delta Wing at Subsonic Speeds

Farhad Ghaffari
Langley Research Center, Hampton, Virginia

July 2005

The NASA STI Program Office . . . in Profile

Since its founding, NASA has been dedicated to the advancement of aeronautics and space science. The NASA Scientific and Technical Information (STI) Program Office plays a key part in helping NASA maintain this important role.

The NASA STI Program Office is operated by Langley Research Center, the lead center for NASA's scientific and technical information. The NASA STI Program Office provides access to the NASA STI Database, the largest collection of aeronautical and space science STI in the world. The Program Office is also NASA's institutional mechanism for disseminating the results of its research and development activities. These results are published by NASA in the NASA STI Report Series, which includes the following report types:

- **TECHNICAL PUBLICATION.** Reports of completed research or a major significant phase of research that present the results of NASA programs and include extensive data or theoretical analysis. Includes compilations of significant scientific and technical data and information deemed to be of continuing reference value. NASA counterpart of peer-reviewed formal professional papers, but having less stringent limitations on manuscript length and extent of graphic presentations.
- **TECHNICAL MEMORANDUM.** Scientific and technical findings that are preliminary or of specialized interest, e.g., quick release reports, working papers, and bibliographies that contain minimal annotation. Does not contain extensive analysis.
- **CONTRACTOR REPORT.** Scientific and technical findings by NASA-sponsored contractors and grantees.

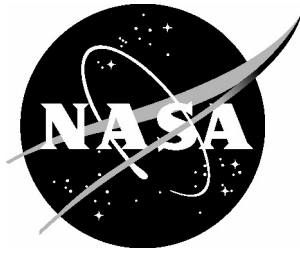
- **CONFERENCE PUBLICATION.** Collected papers from scientific and technical conferences, symposia, seminars, or other meetings sponsored or co-sponsored by NASA.
- **SPECIAL PUBLICATION.** Scientific, technical, or historical information from NASA programs, projects, and missions, often concerned with subjects having substantial public interest.
- **TECHNICAL TRANSLATION.** English-language translations of foreign scientific and technical material pertinent to NASA's mission.

Specialized services that complement the STI Program Office's diverse offerings include creating custom thesauri, building customized databases, organizing and publishing research results ... even providing videos.

For more information about the NASA STI Program Office, see the following:

- Access the NASA STI Program Home Page at [*http://www.sti.nasa.gov*](http://www.sti.nasa.gov)
- E-mail your question via the Internet to [*help@sti.nasa.gov*](mailto:help@sti.nasa.gov)
- Fax your question to the NASA STI Help Desk at (301) 621-0134
- Phone the NASA STI Help Desk at (301) 621-0390
- Write to:
NASA STI Help Desk
NASA Center for AeroSpace Information
7121 Standard Drive
Hanover, MD 21076-1320

NASA/TM-2005-213781



Turbulent Vortex-Flow Simulation Over a 65° Sharp and Blunt Leading-Edge Delta Wing at Subsonic Speeds

Farhad Ghaffari
Langley Research Center, Hampton, Virginia

National Aeronautics and
Space Administration

Langley Research Center
Hampton, Virginia 23681-2199

July 2005

Available from:

NASA Center for Aerospace Information (CASI)
7121 Standard Drive
Hanover, MD 21076-1320
(301) 621-0390

National Technical Information Service (NTIS)
5285 Port Royal Road
Springfield, VA 22161-2171
(703) 605-6000

Contents

| | |
|--|----|
| Summary | 1 |
| Introduction | 1 |
| Symbols | 3 |
| Computational Strategy | 3 |
| Selected geometries and conditions | 3 |
| Numerical method | 4 |
| Computational matrix | 5 |
| Computer platform and method performance | 5 |
| Surface geometry development | 5 |
| Sharp Leading-Edge (SLE) Geometry Analysis..... | 6 |
| Grids and solutions at $\alpha = 13.3^\circ$ | 6 |
| Grids and solutions at $\alpha = 20.5^\circ$ | 9 |
| Effects of angle-of-attack..... | 10 |
| Blunt Leading-Edge (BLE) Geometry Analysis..... | 11 |
| Grids and solutions at $\alpha = 13.3^\circ$ | 11 |
| Grids and solutions at $\alpha = 20.4^\circ$ | 13 |
| Effects of angle-of-attack..... | 14 |
| Concluding Remarks | 15 |
| References | 15 |

Summary

A systematical analysis, with the focus on the prediction of leading-edge flow separation and the ensuing vortex flow characteristics, is presented for a 65° delta wing having either a sharp or blunt leading edge geometry definition. The computational results are based on steady state, turbulent thin-layer, Reynolds-Averaged Navier-Stokes formulation using multi-block structured grid methodology. The numerical analyses are primarily performed for two angles of attack of approximately 13° and 20°, representing a moderately high and a high angle of incident, respectively. All computational results are obtained for free-stream Mach number of 0.40 and Reynolds number of 6 million based on the wing mean aerodynamic chord. The effects of two widely used turbulence models of Baldwin-Lomax with Degani-Schiff modification, and the Spalart-Allmaras, on the numerical results are also presented. In addition, the present computations explore the effects of two numerical flux splitting schemes, i.e., flux difference and flux vector splitting, on the solution development and convergence characteristics. The resulting trends in solution sensitivity to grid resolution for the selected leading-edge geometries, angles of attack, turbulence models and flux splitting schemes are also presented. The validity of the numerical results is evaluated against a unique set of experimental wind-tunnel data that was obtained in the National Transonic Facility at the NASA Langley Research Center.

Introduction

The ability to numerically predict separated flows and the corresponding physics responsible for initiating such a phenomenon has been the subject of research for the past several decades. The fundamental understanding and predictability of the onset of flow separation, across speed regimes, are of paramount importance to almost every aspect of flight aerodynamics, regardless of vehicle class and flight envelope. It can and often does occur over airborne vehicle surfaces, with different degrees of severity, ranging from commercial transport to military and trans-atmospheric aircraft. The occurrence of such separated flows over an airborne vehicle, if not controlled, can have a significant adverse effect on the aircraft aerodynamic performance, stability and control characteristics.

The onset of flow separation can generally be categorized into either a viscous or an inviscid

type. The viscous type occurs primarily on a smooth surface geometry due to the effect of adverse pressure gradient interacting with the boundary layer. As a result, the fluid viscosity provides the essential mechanisms for this type of flow separation to occur and thus its formation is known to be sensitive to the Reynolds number. An example of this type of flow separation is the one that develops on the smooth sided forebodies of an aircraft operating at high angles of attack (Refs. 1-4). Unlike the viscous boundary-layer type, the inviscid type of flow separation occurs at, and primarily induced by, a surface geometry discontinuity. As a result, the separation line, fixed at the surface discontinuity, is known to be relatively insensitive to the Reynolds number. An example of this type flow separation is the one that occurs along the sharp leading edge of a chine forebodies at moderate to high angles of attack (Refs. 5-7).

The off-surface flow characteristics, formed either from a viscous or an inviscid type flow separation, can develop into a stable vortex flow system or a pocket of disorganized, massively

separated, stall type flow structure. Such a vortex flow system often occurs over a slender, military combat aircraft operating at high angles of attack during maneuvering conditions. In general, the occurrence of such vortex flow over the leeward side of an aircraft is advantageous so long as it remains coherent and stable. The low pressure, associated with the core flow of an organized vortex system, induces a suction force over the aircraft neighboring surfaces to generate an additional vortex lift. As an augmentation to its aerodynamic performance characteristics, an aircraft can utilize this vortex lift to enhance its maneuverability. However, with increasing angle of attack, such a coherent vortex system becomes susceptible to instability such as vortex breakdown. The breakdown phenomenon is often associated with a sudden expansion of the vortex core, into a pocket containing reversed flow, thereby causing a significant loss of vortex lift. The occurrence of these instabilities can adversely impact the vehicle's pitching, yawing, and/or rolling moment characteristics and thus the overall flight performance, handling quality and controllability.

The fundamental flow physics and the aerodynamic impacts associated with the flow separation and the resulting vortical flows have been investigated extensively, both experimentally (for example see Refs. 8-13) and numerically (for example see Refs. 14-21). Various delta wing planforms, and in particular with the sharp leading edges, have been used for such investigations. The lack of geometrical complexity for such a wing planform imposes the detail vortex flow physics to be the prime subject for the analysis. Amongst such investigations is a unique and extensive set of experimental database developed for a 65° delta wing with capability to allow for four different leading-edge radii, ranging from sharp to blunt, across a wide range of angle-of-attack, Mach and Reynolds numbers (Refs. 22-25). Subsequent analysis of this database has been used to explore the leading-edge bluntness effects on the onset of flow separation and the resulting vortex flow characteristics (Refs. 26-29). The ability to simulate such effects numerically is a challenging task that is yet to be demonstrated with consistency by the existing Computational Fluid Dynamics (CFD) technology.

The results included in this particular experimental database on the 65° delta wing can also be used to assess the vortex flow prediction capabilities of CFD codes. Two such assessment studies have been conducted. The first numerical analysis was based on Reynolds-Averaged Navier-Stokes (RANS) computations using a multi-block structured grid technique (Ref. 30). The computations were performed primarily at transonic speed and the results indicated some success in predicting the surface loads associated with the vortical flows for various angles of attack and Reynolds number. The second and more recent numerical analysis was designed to demonstrate the flow prediction capability of an unstructured grid method coupled with a grid adaptation technique to better resolve the subject vortical flow at high angles of attack (Ref. 31). The grid adaptation method successfully demonstrated an approach to improve the corresponding suction peak levels with grid adaptation/refinement invoked around the primary vortex core region. This experimental database is also chosen to support the present numerical analysis and the selected geometries and flow conditions will be discussed later in this report.

The primary objective of the present numerical study is to conduct a systematic approach for simulating the leading edge flow separation and the resulting vortical flows on a 65° delta wing having an either a sharp or a blunt leading-edge geometry definition. The computational results are based on an existing state-of-the-art RANS methodology employing multi-block structured grids. The present computational effort will be focused on a free-stream Mach number of 0.40 and a Reynolds number of 6×10^6 based on the wing mean aerodynamic chord along with the assumption that the flow is fully turbulent. In addition to the leading edge geometry variation, the solutions are obtained at a moderately high and a high angle of attack using two different turbulence models and two numerical flux splitting techniques. The effects of grid refinement on solution development and convergence characteristics are also presented to demonstrate the resulting trends towards achieving a more accurate simulation of the subject vortical flow characteristics.

Symbols

| | |
|-------------|--|
| BL/DS | Baldwin-Lomax/Degani-Schiff |
| BLE | blunt leading-edge |
| b/2 | wing reference semispan, 1.0 ft |
| C_L | lift coefficient, $Lift/q_\infty S_{ref}$ |
| C_p | surface pressure coefficient, $(p-p_\infty)/q_\infty$ |
| $C_{p,l}$ | lower surface pressure coefficient, $(p-p_\infty)/q_\infty$ |
| $C_{p,u}$ | upper surface pressure coefficient, $(p-p_\infty)/q_\infty$ |
| CFD | Computational Fluid Dynamics |
| CFL | Courant-Friedrichs-Lewy |
| CFL3D | Computational Fluid Laboratory 3-Dimensional |
| C-O | grid topology, C streamwise and O circumferential |
| c_r | wing root chord, 2.14 ft |
| \bar{c} | wing mean aerodynamic chord, 1.43 ft |
| fds | flux-difference splitting |
| fvs | flux-vector splitting |
| H-O | grid topology, H streamwise and O circumferential |
| i, j, k | computational grid index system in longitudinal, circumferential and radial |
| LaRC | Langley Research Center |
| M_∞ | free-stream Mach number |
| NASA | National Aeronautics and Space Administration |
| \hat{n}_x | surface unit normal in x-axis direction |
| NTF | National Transonic Facility |
| PVC | primary vortex core |
| PVCS | primary vortex core streamlines |
| PVRL | primary vortex reattachment line |
| PVSL | primary vortex separation line |
| p_t | Normalized total pressure, $p_{o,l}/p_o$ |
| p_o | total pressure, lb_f/ft^2 |

| | |
|---------------|--|
| $p_{o,l}$ | local total pressure, lb_f/ft^2 |
| p | local static pressure, lb_f/ft^2 |
| p_∞ | free-stream static pressure, lb_f/ft^2 |
| q_∞ | free-stream dynamic pressure, lb_f/ft^2 |
| RANS | Reynolds-Averaged Navier-Stokes |
| $R_{\bar{c}}$ | Reynolds number, based on \bar{c} |
| S_{ref} | wing reference area, $2.14 ft^2$ |
| SA | Spalart-Allmaras |
| SLE | sharp leading edge |
| SVC | secondary vortex core |
| SVRL | secondary vortex reattachment line |
| SVSL | secondary vortex separation line |
| s | wing local semispan, ft |
| TV | third vortex |
| x/c_r | fraction of wing root chord |
| y/s | fraction of wing local semispan |
| y^+ | inner law distance, $y v^* / \nu$ |
| z/c_r | fraction of wing thickness to wing root chord |
| x, y, z | model reference coordinate system |
| α | angle of attack, degrees |
| v^* | wall friction velocity, $(\tau_w/\rho)^{1/2}$ |
| μ | viscosity, $lb_f \cdot s/ft^2$ |
| ν | kinematic viscosity, μ/ρ , ft^2/s |
| ρ | density, $slug/ft^3$ |
| τ_w | wall shear stress, $(\mu du/dy)_w$, lb_f/ft^2 |

Computational Strategy

Selected geometries and conditions

A preliminary analysis of the available experimental data (Refs. 22-25) was conducted to identify the candidate geometries and the corresponding flow conditions for the present numerical effort. From this analysis, discussed briefly in the next two paragraphs, the two extreme leading-edge bluntness geometries (i.e., sharp and large radius) were chosen for the computational investigation. For simplicity, the

selected geometries will be referred to as the sharp leading edge (SLE) and blunt leading edge (BLE) throughout this report. Similarly, two angles of attack of 13.3° and $\sim 20.5^\circ$, at $M_\infty=0.40$, $R_\infty=6 \times 10^6$ were chosen as the flow conditions for the present computations analysis.

The experimental data was obtained in the National Transonic Facility (NTF) located at the NASA Langley Research Center (LaRC). The tunnel test section is 25 feet long and has a square cross section with a side dimension of 8.2 feet. An overview of the facility and its capabilities can be found in Reference 32. The NTF test was conducted on a sting mounted 65° delta wing model with adaptability to allow for four interchangeable leading edge components, each having different radii (figure 1), and the results have been reported in References 22-25. These reports also provided additional details about the experiment along with discussions on the expected small effects from the tunnel wall interference and aero-elasticity on the measured aerodynamic data. A schematic representation of the subject leading-edge radii, for the different model components, is shown in cross-flow direction in figure 2. The different leading-edge radius contours, designated as sharp, small, medium, and large were normalized by the mean aerodynamic chord of 0, 0.05, 0.15, and 0.30 percent, respectively. The model geometry was designed to have no camber or twist.

The NTF measured surface pressure coefficients for the SLE configuration are shown in Figure 3 for the two selected angles of attack. These results reveal a primary vortex suction peak at all stations. In addition, the results show the variation of the load change with increasing angle of attack along with the inboard movement of the primary vortex suction peak. With one clear exception, similar observations can also be made for the effect of angle of attack on the measured surface loads for the BLE configuration (Figure 4). This exception is the part span flow separation for both selected angles of attack. The results indicate the attached flow characteristics of the load distribution (i.e., only a single low pressure peak occurring on the upper surface, due to the attached flow expansion, around the leading edge) at the span-wise stations of $x/c_r = 0.20$,

0.40, and $x/c_r = 0.20$ for $\alpha = 13.3^\circ$ and 20.4° , respectively. Based on the preliminary analysis of the experimentally measured surface pressure distributions and their significant variations, it is expected that the main numerical challenge here is the prediction of the onset of part span flow separation and its upstream progression with increasing angle of attack for the BLE configuration. Such challenging flow characteristic do not exist on a theoretically SLE configuration because the primary vortex separation line is fixed along the configuration entire sharp leading edge. However, it should be noted that the accurate prediction of the SLE primary vortex strength and location along with the corresponding separation line that forms the secondary vortex flow is not a trivial task.

Numerical method

The numerical analysis is performed with a multi-block, structured-grid method known as CFL3D (Ref. 33). Its most recent released version 6.1 is employed throughout the present study. The numerical method is well documented and has been extensively validated for a variety of applications with different classes of flows and configurations. The algorithm is based on the compressible, time-dependent, RANS equations that are written in a curvilinear coordinate system. A cell-centered, finite volume approach is used to solve the equations in a conservative form. The integral form of the conservation equations is given by

$$\frac{\partial}{\partial t} \iiint \hat{Q} dV + \iint \hat{f} \cdot \hat{n} dS = 0$$

where the time rate of change ∂t of the state vector \hat{Q} within a cell volume dV is balanced by the net flux \hat{f} across the cell surface dS with a unit normal \hat{n} . An upwind-biased, flux-difference-splitting (fds) scheme (Ref. 34) or flux-vector splitting (fvs) approach (Ref. 35) is used to solve the inviscid terms whereas central differencing is applied to represent the viscous terms.

Numerous turbulence models, from algebraic equation model to one and two equation models, have been incorporated into the code. The method

uses implicit time advancement with ability to simulate both steady and unsteady flows. Both multi-grid and mesh sequencing techniques are implemented for accelerating solution convergence. Multi grid-block topologies are allowed having either planar or non-planar interfaces in the physical domain. The flow primitive variables are interpolated across the various block interfaces using a searching technique based on a combination of linear and polynomial equations (Ref. 36).

Computational matrix

A variety of available options in CFL3D were considered to identify those features that could have an impact in predicting the subject vortical flow over the chosen geometries and flow conditions. For this initial assessment study, it was decided to investigate the effects of two turbulence models and two flux splitting techniques. The selected turbulence models are the Baldwin-Lomax (Ref. 37) with Degani-Schiff modification (Ref. 38) and the Spalart-Allmaras model (Ref. 39). These two turbulence models have been chosen because the applications of more advanced two-equation turbulence models have been reported to excessively diffuse vortical flows for highly swept slender wing configurations (for example see Refs. 18-19, and 40-41). In addition, the two chosen numerical flux-splitting schemes are the flux difference splitting (fds) and the flux vector splitting (fvs). The combination of the selected delta wing geometries and flow conditions along with the identified CFL3D features of interest formed the computational matrix for the present numerical investigation (Table1).

| Geometry | SLE | | BLE | |
|------------------|-------|-------|-------|-------|
| | 13.3° | 20.5° | 13.3° | 20.4° |
| Turbulence model | BL/DS | SA | BL/DS | SA |
| Flux splitting | fds | fvs | fds | fvs |

Table 1. Selected geometries, flow conditions, and CFL3D features.

The results presented in this report are all obtained, based on a time dependent, fully turbulent, thin-layer approximation to the RANS

equations. The multi-grid and mesh sequencing techniques were invoked to accelerate the solution convergence to a steady state. In addition to addressing the solution dependency to grid resolution, the experimental data is used to gauge the accuracy of the numerical predictions. As mentioned earlier with respect to the expected small effects due to the wall interference and aero-elastic on the measured data, all present computations are performed for free air (i.e., wind-tunnel walls are not numerically modeled).

Computer platform and method performance

The computations were performed on a desktop SGI Octane with a single 270 MHz processor or on a single 250 MHz processor of an Origin-2000, each having 250×10^6 words of memory. The solutions were initiated from free stream conditions and generally advanced in using 3-levels of mesh sequencing along with the 3 multi-grid V-cycle. An initial Courant-Friedrichs-Lewy (CFL) number of 0.1 was used and ramped up linearly to 3 over the first 200 iterations. Otherwise noted, the solutions were generally obtained over 2000, 1000, and 1000 iterations on the coarse, medium, and fine grids, respectively.

A typical solution with the BL/DS turbulence model coupled with the fds or fvs scheme required about 80 and 230 $\mu\text{sec}/\text{cell}/\text{iteration}$, respectively. Whereas, a typical solution with the SA model coupled with the fds or fvs method required about 100 and 250 $\mu\text{sec}/\text{cell}/\text{iteration}$, respectively. The flow solver required about 32 words of memory per cell on such computer platforms. The memory limitations on the available computers restricted the maximum computational grid size to about 6.5×10^6 points which required $\sim 200 \times 10^6$ words of total memory.

Surface geometry development

The surface geometry of the delta wing model along with the near-field sting is defined analytically as discussed in detail in Reference 22.

The planform view of the initial wire-frame geometry along with the truncated representation of the sting is shown in Figure 5. This figure also shows the geometry coordinate axes system (x , y , and z) as well as a few selected reference dimensions of interest. The model dimensions in the numerical simulations are normalized with respect to the wing root chord and the corresponding values are shown in the parentheses in figure 5. The wing geometry can be broken down into three main parts, the interchangeable leading-edge component, the trailing-edge closure component, and the flat plate region having a constant thickness (thickness/ $c_r=0.034$), as shown on the lower half planform view of the geometry in Figure 6. The apex and the trailing edge of the flat plate region are located at $x/c_r=0.15$ and 0.90 , respectively. The upper half of the figure 6 shows the initial wire-frame geometry along with the five span-wise stations where the experimental surface pressure coefficients were measured.

The initial wire-frame geometry, for both the sharp and the blunt leading-edge configurations, was analytically defined with emphasis on clustering points around regions of the surface with high curvature. As a result, a typical cross section was generally described with 104 points from which 100 points were used to define the interchangeable leading-edge component and 4 points to represent the flat plate region of the wing (i.e., 2 points for the upper surface and 2 points for the lower surface extreme inboard and outboard locations). Similarly, the initial wire-frame geometry definition consisted of 25 longitudinal stations in axial direction from which 17 were distributed aft of the flat-plate region with clustering at the wing trailing edge.

The x -component planform views of the surface unit-normal (i.e., \hat{n}_x) variation for both the SLE and BLE geometries are shown in the lower part of figure 7. Note the smooth variation and the similarity of the \hat{n}_x distribution for both geometries. In addition, the upper part of the figure shows a typical wire-frame cross-sectional definition ($x/c_r = 0.60$) and the trailing-edge closure section ($2y/b=0.60$) for both

configurations. Finer plot scales are used in vertical axis than the horizontal axis to highlight the sensitivity of the geometry coordinates in the z -axis direction.

Sharp Leading-Edge (SLE) Geometry Analysis

Grids and solutions at $\alpha = 13.3^\circ$

This section describes the initial sets of numerical surface and volume grid generation along with the corresponding results and analysis. Although three different surface and volume grid strategies are discussed first, the numerical solutions and the analyses from each grid were used to improve the subsequent grid in an evolving process. Such a process is necessary because of lack of grid adaptation capability for body conforming structured grid RANS methodology, in general, including the present numerical method.

The first grid used in the present study incorporated five longitudinally patched blocks, three over the wing and two for the sting. The developed wire-frame geometry, discussed earlier, was used as the initial database for distributing points to generate the computational surface grid definition. The planform view of the computational surface definition for the first grid developed for the sharp leading-edge configuration, designated as SLE1, is shown in figure 8. The surface grid points were distributed on the upper and lower surface symmetrically about the wing chord plan. The wing surface grid distribution was designed to accommodate three longitudinally patched blocks with grid clustering at the leading edge, trailing edge, sting-wing juncture, and block boundaries. The first block was designed, with a C-O grid topology, to wrap around the nose up to the longitudinal station $x/c_r=0.15$ (apex point of the wing flat plate region). The second and third blocks were designed to have an H-O grid topology. As shown in figure 8, the surface grid dimensions in longitudinal direction (x -axis, i -index) and circumferential direction (y -axis, j -index) were 25×49 , 25×145 , and 33×193 for block 1, block 2,

and block 3, respectively. The longitudinal grid i -index starts at the wing apex whereas the circumferential grid j -index begins on the upper surface along the plane-of-symmetry.

A volume grid was generated with an in-house developed code that is based on transfinite interpolation and has been successfully applied to various configurations in the past (for example see Ref. 3). An oblique far-field view of the overall volume grid is shown in figure 9. The far-field boundaries were extended to about $10c_r$ from the wing surface geometry in the upstream, radial, and downstream directions. All the present computations were obtained using the plane-of-symmetry assumption along with invoking the characteristic boundary condition on the far-field outer boundary and the volume grid outflow plane. Similarly, the singular axis using half-symmetry boundary condition was used to model the singularity axis in the C-O grid-block topology. Although, this particular volume grid is for SLE1 case, this overall volume grid strategy and topology was generally used throughout the present computational analysis.

The near-field view of the SLE1 volume grid is shown in figure 10. This figure shows the close-up view of the C-O grid around the wing apex followed by four H-O grid blocks; two over the remainder of the wing and two for the model sting geometry. The volume grid consisted of 65 points in the radial direction in all blocks with the exception of near-field trailing-wake block 4 that had 97 points. The additional radial points in the near-field trailing-wake block 4 were designed to accommodate the clustering of the grids for better resolution and the downstream propagation of the wake flow-field properties. Such trailing-wake flow properties include the wing leading-edge shear-layers (due to flow separation) and the trailing wake system that forms from the wing surface viscous boundary layer. The SLE1 volume grid consisted of about 1×10^6 points and the numerical results indicated an average $y^+ \sim 0.3$ was achieved for resolving the turbulent boundary layer in the laminar sub-layer region over the wing.

A second grid was devised, designated as SLE2, based on the lessons learned from SLE1

solutions and analyses. This new grid combined the first two blocks of SLE1 into a single C-O grid that is more topologically consistent with the expected conical-like vortex-flow structures. The effect of this change on the surface grid distribution, relative to the SLE1, is shown in figure 11 from a planform vantage point. Similar to SLE1, the new surface grid distribution was generated with the emphasis on clustering points at the wing leading edge, trailing edge, wing-sting juncture, and block boundaries. It should be noted that the new surface grid contains finer longitudinal definition at the apex compared to SLE1. This is due to the elimination of the block 1 and block 2 boundary in SLE1 grid and thus the un-needed finer longitudinal point distribution. The near-field view of the volume grid for the SLE2 having a total of 4 blocks is shown in figure 12. The grid points in the radial direction were doubled compared to SLE1 with the exception of the aft trailing-wake block. The SLE2 volume grid consisted of about 2×10^6 points and the numerical results indicated a similar average y^+ values over the wing as the SLE1 grid. As a result, the new volume grid generally contained finer point distribution in the field for better resolution of the expected off-surface flow characteristics.

A third grid was developed to have an even finer grid distribution in the radial direction than the SLE2 grid. This new grid, designated as SLE3, employed the same SLE2 surface grid definition, but combined the two trailing wake blocks into a single H-O topology block. The near-field view of the volume grid for the SLE3 is presented in figure 13. As a result, the SLE3 contained a total of three grid blocks and the new single trailing-wake block is expected to allow for a better propagation of the wake system downstream to the outflow plan. The SLE3 volume grid consisted of about 3×10^6 points and the numerical results indicated an average $y^+ \sim 0.7$ was achieved for resolving the turbulent boundary layer over the wing. The radial grid stretching ratio for all three volume grids was generally between ~ 1.10 to ~ 1.20 .

Initial sets of numerical calculations were performed at $\alpha=13.3^\circ$, $M_\infty=0.40$, and $R_c=6 \times 10^6$

using the SLE1, SLE2, and SLE3 volume grids. These computations utilized the Baldwin/Lomax turbulence model with the Degani/Schiff modification and employed the van-Leer's flux vector-splitting scheme. For simplicity, this combination of turbulence model and flux splitting option will be denoted as BL/DS-fvs in the key caption of the figure. Similar denotation scheme will be used for other combination of turbulence model and flux splitting technique throughout this report.

The computed surface pressure coefficients along with the corresponding experimental data are shown in figure 14 for the five span-wise stations over the wing. As discussed earlier, the experimental pressure distributions indicate the presence of a suction peak at all stations that can be attributed to the low pressure associated with the leading-edge primary vortex flow. This primary vortex suction peak is also featured in all the computational results. However, note the significant change in the computed surface C_p distributions between the results obtained from the SLE1 grid, and those obtained from the SLE2 and SLE3 grids. The small change in the computed surface C_p distributions, obtained from SLE2 and SLE3 grid, suggests that a reasonable grid independent solution has been achieved. The results indicate an improved correlation between the computed surface C_p using SLE3 grid and the experimental data at all span-wise stations.

Based on these results, the SLE3 volume grid was chosen to investigate the effects of turbulence models and flux splitting schemes on the numerical predictions. Numerical solutions were obtained at $\alpha=13.3^\circ$ with the BL/DS and SA turbulence models using either the fvs or fds. The computed results for surface flow properties are shown in figure 15 from a planform vantage point. The plotted surface flow properties include the computed surface pressure coefficient contours along with surface flow streamline patterns. In general, the flux splitting scheme appears to cause only a small change on the surface flow properties with either turbulence model. However, the influence of different turbulence models on the surface flow streamline patterns and the surface pressure coefficient contours appears to be significant using either

flux splitting schemes. The surface pressure coefficient contours computed with the SA model generally show a lower suction-peak level in magnitude that is spread out over a wider span than the corresponding results with the BL/DS model. In addition, the predicted secondary vortex separation line (SVSL) and the corresponding secondary vortex reattachment line (SVRL) appear to be more pronounced in the BL/DS solution than those computed with the SA model. It should also be noted that, with only a minor difference, all the computed surface flow properties indicate the presence a low-pressure band that is roughly parallel to the wing trailing edge followed by a flow separation line near the wing trailing edge closure region (see figure 6 for model description).

The computed flow features are presented in figure 16 from an oblique front view of the upper surface. The off-surface flow characteristics are represented by the normalized total-pressure contours ($p_t=p_{o,i}/p_o$) at various cross-flow planes along with the primary vortex-core streamline (PVCS) traces. Each PVCS trace is generally calculated, from their respective origin located in a cross-flow grid plane over the wing at about mid-chord station, in both upstream and downstream direction. The normalized total-pressure contours are shown at the cross-flow grid planes that correspond to the span-wise stations where the experimental surface C_p were measured, except the last plane where it is shown at the wing trailing edge (i.e., $x/c_r=1.0$). This figure also shows a typical cross-flow normalized total-pressure contours over the wing trailing wake region (i.e., $x/c_r=1.36$). This format for presenting the computed surface and off-surface flow properties will be used throughout this report.

The comparison of the numerical results in figure 16 suggests that the SA turbulence model generally predicts a larger primary vortex flow structure along with a more diffused vortex core (i.e., higher levels of p_t that is indicative of lower viscous loss). To illustrate this effect, the near field cross-flow view of the results at station $x/c_r=0.60$ are shown in figure 17. The figure also shows the truncated computational grids in the radial direction ($k=120$) only on the lower half of

the configuration for reference. It can be observed from these results that the entire vortical flow structure at this station is captured with about 120 radial grid points. The comparison of the results also indicate that the BL/DS turbulence model predicts a much tighter p_t contours in the primary vortex along with a more clearly defined secondary vortex flow structures. Unlike the solution with the SA turbulence model, the results with the BL/DS model also reveal the presence of an unexpected third vortex (TV), with the same rotational sense as the primary vortex, located between the secondary vortex and the wing leading-edge. This third vortex has a coherent vortex core and persisted from the wing apex region to the trailing edge.

The effects of different turbulence model and flux splitting on the computed surface pressure coefficients at $\alpha=13.3^\circ$, using the SLE3 volume grid, are shown in figure 18. Regardless of which flux splitting schemes are used, the results generally indicate that the SA turbulence model predict lower suction peak levels (more positive value) at all stations and that the primary vortex reattachment line is generally predicted further inboard. The computed results with the BL/DS model reveal a much better correlation with the experimental data, particularly with the fvs approach in predicting the pressure levels in the secondary vortex flow region.

The influence of turbulence models and flux splitting on the solution residual history (i.e., $\log(\text{residuals})$) and the overall C_L at $\alpha=13.3^\circ$, using the SLE3 volume grid, are shown in figure 19. The convergence characteristics for all the solutions generally indicate about a 6 orders-of-magnitude drop in the residuals and a negligible oscillation in the overall lift coefficient over the last 200 fine-grid iterations. The magnitude of the oscillation in overall C_L varied from case to case and the corresponding values are denoted in the figure. The solutions with the fds scheme generally required additional fine grid iteration to achieve similar levels of solution convergence as those computed with the fvs approach.

Grids and solutions at $\alpha = 20.5^\circ$

The SLE1, SLE2, and SLE3 volume grids were employed to compute the flow at $\alpha=20.5^\circ$ using the BL/DS turbulence model coupled with the fvs scheme. The computed surface pressure coefficients along with the corresponding experimental data are shown in figure 20. The numerical results indicate a better correlation with the experimental data with increasing grid resolution in capturing the primary vortex suction peak levels. However, this effect appears to deteriorate in the aft stations. Subsequent flow field analysis of the results, based on the SLE3 grid, revealed the presence of a vortex breakdown and will be discussed later. In addition, the disagreement between the computational prediction and the experimental data also evident in the secondary vortex flow region at $x/c_r=0.40$ and 0.60 stations. The results from this analysis clearly indicate that the existing grids are not adequately resolving the correct flow characteristics. As a result, a forth volume grid was generated, designated as SLE4, to address the existing anomalies.

Three main factors contributed to the development of various modification made in the new SLE4 grid. The first factor was driven by the surface pressure disagreements shown between the computational results and the data in the secondary vortex flow region around the wing mid-chord stations. The secondary vortex flow separation generally occurs on the surface due to the strong span-wise flow deceleration induced by the primary vortex. Accurate prediction of such span-wise flow separation line generally requires fine surface grids in the circumferential direction. As a result, the SLE3 surface grid was modified to incorporate 96 additional points in the circumferential direction while maintaining the similarity of the point distribution. The effect of this grid modification on the surface point distribution is shown in figure 21 relative to the SLE3 grid. The second factor was driven by the lack of a good surface pressure correlation between the experimental data and the predictions in the aft part of the wing. In an attempt to better resolve the aft wing flow characteristics, an alternative approach in modeling the trailing wake

grid block was adopted. This new wake grid maintains the same H-O grid topology, as used over the aft wing, but includes a zero-thickness plane that extends downstream from the wing trailing edge along its chord plane. A flow through boundary condition is used to simulate the flow across this wake plane. Finally, the third factor dealt with establishing the number of grid points and distribution in the radial direction. Based on the results from SLE2 and SLE3 (see figure 20), it was decided to apply 169 radial number-of-points for block 1 (i.e., compromise between SLE2 and SLE3) along with maintaining the same number of radial points in block 2 as that of the SLE2 grid.

The SLE4 volume grid consisted of three blocks with grid dimensions of $49 \times 241 \times 169$, $33 \times 289 \times 129$, and $49 \times 289 \times 129$. The overall volume grid contained about 5×10^6 points and the near-field view of the grid is shown in figure 22. This grid was used to compute the flow at $\alpha = 20.5^\circ$ with the BL/DS turbulence model and flux vector splitting scheme. The numerical results indicated an average $y^+ \sim 0.6$ was achieved for resolving the turbulent boundary layer over the wing.

The effects of grid modifications on the predicted flow features, relative to the SLE3 results, are presented in figure 23. The results with the SLE3 grid revealed, as mentioned earlier, the presence of a primary vortex burst to occur over the aft wing region. A solid surface, shown in purple color, is used in the figure to highlight the corresponding vortex burst region (i.e., $u_x \leq 0$). The most significant effect of the grid modification on the computed flow features is clearly the elimination of this vortex burst phenomenon. The near field view of the cross-flow normalized total pressure contours at station $x/c_r = 0.60$ is shown in figure 24 for both the SLE3 and SLE4 solutions. The figure also shows the truncated computational grids in the radial direction for both the SLE3 ($k=110$) and the SLE4 ($k=120$). The comparison of the two grids illustrates that, despite the lower total number of radial grid points, the SLE4 provides more points in the near field region. This effect, indicative of strong clustering of the points, in the SLE4 grid along with the increased number of points in the

circumferential direction is expected to better grid resolve the primary and secondary vortex flow structures.

The effects of grid modifications on the computed surface pressure coefficients at $\alpha = 20.5^\circ$, using both the SLE3 and SLE4 grids, are shown in figure 25. The results indicate that SLE4 solution indeed provides an improved correlation with the experimental data, particularly at the last two stations that suggests the vortex burst in the SLE3 solution was grid induced. The effect grid modification on the solution residual history and the overall C_L , using the SLE3 and SLE4 grids, are shown in figure 26. The convergence characteristics for both solutions generally indicate about a 5 to 6 orders-of-magnitude reduction in the residuals and a negligible oscillation in the overall lift coefficient over the last 100 fine-grid iterations. Note that the solution with SLE4 grid produced a relatively larger oscillation in C_L (i.e., ± 0.001) compared to the SLE3 solution.

Effects of angle-of-attack

The ability of the method to predict the flow characteristics and the resulting incremental effects on the selected angles of attack for the SLE configuration is discussed in this section. To insure grid consistency for addressing this effect, the SLE4 was used to compute the flow at $\alpha = 13.3^\circ$ using a similar solution development process as the one used earlier for $\alpha = 20.5^\circ$ case. The computed surface pressure coefficients based on the SLE4 grid produced almost identical corresponding C_p distributions as those shown earlier using the SLE3 grid (see figures 14 and 18). The convergence characteristics for the new solution revealed an approximately 6 orders-of-magnitude drop in the residuals and limited oscillations in C_L to about ± 0.0001 over the last 200 fine grid iterations.

The effects of angle of attack on the computed flow characteristics, using the SLE4 grid, are presented in figure 27. The results indicate the expected general trend, resulting from the increase in angle-of-attack, on the predicted flow features. This expected trend is the production of

a larger primary vortex flow system with an increased viscous loss in the core (i.e., lower p_t values) that results in a higher suction peak footprint on the surface. Furthermore, the surface flow streamline patterns also show the inboard movement of the PVRL, SVSL, and SVRL with increasing angle-of-attack.

The effects of angle-of-attack on the computed surface C_p distributions and the correlation with the experimental data for the SLE configuration are presented in figure 28. The comparison of the results indicates a reasonably good agreement between the predictions and the measurements on the upper surface regions associated with both the primary and the secondary vortex flows. Such a comparison of the results also shows an excellent agreement for the predicted and measured surface pressure coefficients on the lower surface at all five semi-span stations.

Blunt Leading-Edge (BLE) Geometry Analysis

Grids and solutions at $\alpha = 13.3^\circ$

The initial BLE grid, designated as BLE1, was generated to have the same number of surface grid points and distributions, in both the longitudinal and circumferential directions, as the SLE4 grid. Figure 29 qualitatively illustrates the similarities between the two surface grid definitions such as the overall grid topology and the corresponding point distributions. A flow field volume grid was generated with this initial surface grid and the corresponding near-field view is shown in figure 30. The volume grid contained the same blocking strategy as used for the SLE4. The overall grid consisted of about 4.6×10^6 points having three blocks with grid dimensions of $49 \times 241 \times 129$, $33 \times 289 \times 129$, and $49 \times 289 \times 129$.

For the purpose of comparison, a close-up view of a typical cross-flow grid ($x/c_r = 0.20$) from both the BLE1 and the SLE4 grid are superimposed and shown in figure 31. The circumferential points are distributed based on the local sectional arc-length to maintain grid consistency around the leading edge between the

two geometries. The most significant difference between the two grids is the introduction of a finer radial point distribution in the BLE near-field region to better resolve the blunt leading-edge viscous boundary layer. A sample representation of this effect is illustrated, in the close-up view, for the wing leading edge region in the lower left corner of figure 31. For example at this typical cross-flow plane, there are 13 and 18 points, over a $\Delta (y/c_r) = 2.3 \times 10^{-5}$ local span along a radial grid line emanating from the surface leading-edge point (i.e., $x/c_r = 0.20$, $y/c_r = 0.0932615$, $z/c_r = 0.0$), for the SLE4 and BLE1 grids, respectively. The cell height distribution along the radial grid lines generally employed a stretching ratio of ~ 1.1 in both the SLE4 and BLE1 grids. The numerical solutions indicated an average $y^+ \sim 0.3$ was achieved for resolving the wing turbulent boundary layer.

The BLE1 grid was employed to compute the flow at $\alpha = 13.3^\circ$ with all the possible combinations between the BL/DS, SA, fds, and fvs scheme. The computed surface pressure coefficients along with the corresponding experimental data are shown in figure 32 for the five wing stations. The measured upper surface pressure distributions clearly indicate a part span flow separation with the first inboard (from the leading-edge) suction peak occurring over the wing at station $x/c_r = 0.60$ that can be attributed to a form of leading-edge vortex flow. Such a surface C_p suction peak does not exist at the station $x/c_r = 0.40$ which implies that the leading-edge flow separation ought to occur somewhere between the two stations.

The computed results obtained with the BL/DS turbulence model indicate a fully attached flow over the wing at all stations, regardless of which flux-splitting scheme is employed. Similar to the experimental data, the numerical solutions with the SA turbulence model also indicate a part span leading-edge flow separation. However, the origin of this leading edge flow separation appears to occur at a station further downstream than the corresponding experimental data. Clearly, the computational results with the SA turbulence model provide a better correlation with the experimental data than those predicted by the BL/DS model.

The effects of turbulence models on the computed flow features are shown in figure 33. The solutions based on the fvs technique are only shown because the fds results were almost identical. The figure clearly reveals a significant effect, resulting from the turbulence model, on the computed flow features. As discussed earlier in conjunction with the computed surface C_p analysis, the BL/DS solution predicts a fully attached flow over the entire wing upper surface, whereas, the SA results indicate a part span leading edge flow separation that forms a vortex flow over the aft-wing region. It is interesting to note that the initial leading-edge flow separation occurs on the upper surface, upstream of station $x/c_r=0.60$, and then it moves towards the wing leading edge further aft as it approaches the trailing edge. Though difficult to see in this figure, these results also indicated the presence of a flow separation line, similar to those shown earlier for the SLE solutions, over the trailing-edge closure region (see figure 15).

The effects of turbulence models and flux splitting schemes on the solution residual history and the overall C_L are shown in figure 34. The convergence characteristics for all solutions generally indicate about 5 to 6 orders-of-magnitude drop in the residuals and a negligible oscillation in the overall lift coefficient over the last 200 fine-grid iterations. However, the solution with the BL/DS model using the fvs technique was stopped after ~ 500 fine grid iteration, at the expense of saving computational time, because the ongoing analysis indicated a fully attached flow characteristic with a reasonable level of convergence criterion.

The existing BLE1 grid was modified to incorporate finer point distribution in the radial direction. Two new volume grids, designated as BLE2 and BLE3, were sequentially generated to have slightly coarser radial grid distribution in the boundary layer region in order to propagate more points in the field to better resolve the off-surface flow characteristics. The BLE2 volume grid consisted of about 6×10^6 points in three blocks with grid dimensions of $49 \times 241 \times 169$, $33 \times 289 \times 169$, and $49 \times 289 \times 169$. Similarly, the BLE3 volume grid contained about 6.5×10^6 points in three blocks with grid dimensions of

$49 \times 241 \times 193$, $33 \times 289 \times 193$, and $49 \times 289 \times 169$. Numerical solutions with both the BLE2 and BLE3 grids revealed an average $y^+ \sim 0.9$ was attained for resolving the wing turbulent boundary layer flow characteristics. It should also be noted that memory limitations, associated with the available computer resources, restricted the maximum number of grid points in the present computational analysis to about what is employed in the BLE3 grid.

The new BLE2 and BLE3 grids were used to compute the flow with the SA turbulence model coupled with the fds or the fvs schemes. The computed surface pressure coefficients along with the corresponding experimental data are shown in figure 35. The comparison of the computed and measured data indicates an improved correlation with grid refinement particularly at the last two stations. However, such good improvements in the correlation are not evident for the station $x/c_r=0.60$. Furthermore, the computed surface C_p with the fvs scheme is found to generally provide a better correlation with the experimental data over the last two stations.

The predicted flow features using the BLE3 grid along with the earlier results computed with the BLE1 are presented in figure 36. Both solutions are obtained with the SA turbulence model coupled with the fvs scheme. In general, the effect of grid refinement on the computed flow characteristics can be summarized into two features. The finer BLE3 grid solution appears to produce a larger primary vortex flow structure, particularly near the trailing edge, along with different flow separation line patterns. Such different separation line patterns can generally be described as the outboard movement of the primary vortex separation line towards the wing leading edge along with what appears to be a form of a SVSL aft of the station $x/c_r=0.80$.

The effects of grid modifications on the solution residual history and the overall C_L for both the BLE2 and BLE3 grids are shown in figure 37. These solutions were obtained by adopting a slightly different approach in terms of the number of iterations used during the coarse, medium and fine grid cycles. The convergence characteristics for all the solutions generally

indicate about a 6 orders-of-magnitude drop in the residuals and a negligible oscillation in the overall lift coefficient over the last 100 fine-grid iterations.

Grids and solutions at $\alpha = 20.4^\circ$

The initial BLE1 grid was employed to compute the flow at $\alpha=20.4^\circ$ using the BL/DS or SA turbulence models coupled with the fds or the fvs techniques. As shown in figure 38, the solutions for this particular case was the most difficult to achieve with the same level of convergence characteristics and consistency relative to the previous solutions. For example, the solution with the BL/DS model using the fds scheme experienced convergence difficulties over the fine grid solution development (see the plot in the upper right quadrant of figure 38) and thus the numerical predictions will not be included in the subsequent data analysis. Such convergence difficulties included a large oscillation in the computed C_L (about ± 0.02) along with the lack of a good residual history (only about 4 orders of magnitude drop). Furthermore, the solution with the SA model coupled with the fvs scheme also experienced convergence problems, not with respect to the computed C_L , but rather on the residual as shown in the lower left quadrant of figure 38. The solutions with the BL/DS turbulence model using the fvs scheme along with the SA model employing the fds method provided relatively the best overall convergence characteristics.

The computed surface pressure coefficients along with the corresponding experimental data are shown in figure 39 for the five wing stations. The experimental surface C_p distributions indicate the presence of a suction peak, which can be attributed to the leading edge primary vortex flow, over the entire wing with the exception of the first station. The experimental data at the first station indicate an attached flow like surface C_p distribution. With some small differences, all the computed results generally agree well with the experimental data over the entire wing. The small differences in the computational results appear to be due to the turbulence modeling effects, particularly at the station $x/c_r=0.40$. At this

station, the BL/DS model seems to better capture the primary vortex suction peak level, as well as the character of the pressure distribution that occurs approximately over the range $0.40 < y/s < 0.70$. With the exception of the station $x/c_r=0.40$, however the SA solutions generally indicate a better agreement with experimental data regardless of which flux splitting technique is used.

The effects of turbulence models and flux splitting method on the computed flow features, using the BLE1 grid, are presented in figure 40. The predicted flow features, based on the SA model with either flux splitting schemes, generally reveal a part span leading-edge flow separation that originates at $x/c_r \sim 0.30$. The resulting flow separation leads into the formation of a coherent and stable primary vortex flow system. The comparison of the results, obtained with different turbulence model based on the fvs, indicate similar flow characteristics for the most part, with one clear difference. This difference between the two solutions occurs in the core region of the predicted primary vortex flow. Unlike the solutions with the SA model, the BL/DS results revealed the presence of a vortex burst near the wing trailing edge region.

A detail examination of the computed flow characteristics, based on the BL/DS turbulence model, revealed the existence of a weak bubble like flow separation over the wing apex region (i.e., $x/c_r \leq 0.40$). This small pocket of separated flow, not as well organized with a core structure in the SA solutions (see figure 41), appears to get entrained into the main wing leading-edge primary vortex flow aft of the station $x/c_r=0.40$. It can be deduced from figure 41 that this bubble like flow separation is captured with roughly about 70 radial grid points. The presence of this flow phenomenon is primarily responsible for the good agreement, shown earlier in figure 39, between the computed and the measured surface C_p distribution at station $x/c_r=0.40$ over the range $0.40 < y/s < 0.70$. In addition, the comparison of the results shown in figure 41 at $x/c_r=0.40$ indicates that the BL/DS model predicts a smaller size primary vortex with a tightly formed core p_t contours that is located slight outboard (from the

fixed radial grid-line at $j=67$) relative to the solution with the SA model.

In an effort to address the solution sensitivity to grid refinement, a new grid designated as the BLE2n was generated using the BLE1 surface grid definition. The new grid incorporated additional number of points in the radial direction to better resolve the off surface flow field. The final BLE2n volume grid consisted of about 6.5×10^6 points in three blocks with grid dimensions of $49 \times 241 \times 193$, $33 \times 289 \times 193$, and $49 \times 289 \times 169$. This grid was used to compute the flow at $\alpha=20.4^\circ$ based the BL/DS turbulence model using the fvs and the SA model coupled with the fds scheme. These new solutions revealed an average $y^+ \sim 0.7$ was attained for resolving the wing turbulent boundary layer. The convergence characteristics for the BLE2n solutions are presented in figure 42. The convergence history indicates that the solution with the SA turbulence model using the fds diverges in the fine grid solution development. Subsequent analysis, based on individual grid block convergence history, indicated the diverging effects were initiated, over the trailing wake (i.e., block 3) and aft-wing (i.e., block 2) regions, during the medium grid solution development. The solution convergence history, based on the BL/DS model using the fvs scheme, shows good overall characteristics in both the residual and the oscillations in the computed C_L .

The computed flow features, based on the BL/DS model and the fvs, are presented in figure 43 along with the earlier BLE1 results. The effects of grid refinement on the computed flow features appear to be generally small, except in the primary vortex core region. The solution with the finer BLE2n grid reveals a larger burst region in the primary vortex core with an origin that is initiated further upstream. The existence of this flow phenomenon in the present steady state computation is surprising despite the fairly well behaved and reasonable convergence characteristics (see figure 42). The effects of grid refinement on the computed flow features over the wing apex region (i.e., $x/c_r=0.2$ and $x/c_r=0.40$) are contrasted against the earlier BLE1 results in figure 44. The results with the finer BLE2n grid generally show a similar off surface flow

characteristics with respect to the separated bubble. However, the contrast between the two solutions at the station $x/c_r=0.40$ indicates that the finer grid promotes a slight inboard movement of the primary vortex core location (relative to the fixed radial grid-line at $j=67$).

The effects of grid refinement on the computed surface pressure coefficients are presented in figure 45 along with the corresponding experimental data. The comparison of the results indicates, though generally small, that the solution with the finer BLE2n grid causes a slight inboard movement of the primary vortex suction peak. This effect produces, for the most part, a better correlation with the corresponding experimental data, particularly at the station $x/c_r=0.40$. It is also important to note that, in spite of the presence of a vortex burst region in both solutions, the predicted suction peaks associated with the primary vortex flow are higher (more negative) than the experimental data, particularly at the station $x/c_r=0.95$. Such an effect along with the relatively good comparison, between the predictions and the data, at the upstream stations (i.e., $x/c_r \leq 0.80$) suggest that the predicted flow features may indeed be close to the experimental flow field.

Effects of angle-of-attack

The effects of increase in angle of attack on the computed flow features for the BLE configuration are presented in figure 46. As expected, the results indicate significant effects on the overall flow characteristics. Such effects can generally be summarized by the upstream progression of the leading-edge flow separation, larger primary vortex system along with a better formation of the SVSL and the corresponding SVRL. Unlike the solution at $\alpha=13.3^\circ$, an observation can be made that the PVSL for the high angle of attack is initiated closer to the leading edge rather than on the upper surface.

The incremental effects due to the increase in angle-of-attack on the computed surface C_p and the correlation with the experimental data are presented in figure 47. The comparison of the results shows that such effects are predicted reasonably well on the upper surface with the

exception results at $x/c_t=0.60$ for $\alpha=13.3^\circ$. The predictions of the incremental effects are excellent on the lower surface.

Concluding Remarks

Steady state, turbulent thin-layer, Reynolds-Averaged Navier-Stokes solutions, based on a multi-block structured grid methodology, are presented for a 65° delta wing having either a sharp leading-edge (SLE) or blunt leading-edge (BLE) geometry definition. The computations are primarily performed at $M_\infty=0.40$, $Re_c=6 \times 10^6$, for two angles of attack of 13.3° and $\sim 20.5^\circ$. The numerical results are obtained, using a systematical approach, to assess the prediction capability of the method for simulation the leading-edge flow separation and the ensuing vortex flow characteristics. The aerodynamic effects of two widely used turbulence models of Baldwin-Lomax with Degani-Schiff (BL/DS), and the Spalart-Allmaras (SA), on the computational results are addressed. In addition, the effects of two flux splitting techniques, i.e., flux difference splitting (fds) and flux vector splitting (fvs), on the solution accuracy and convergence characteristics are also evaluated. The resulting trends in the solution sensitivity to grid resolution for the selected leading-edge geometries, angles of attack, turbulence models, and flux splitting schemes are analyzed and correlated with the experimental data.

The SLE results based on the BL/DS model revealed the presence of a third vortex, in addition to the expected primary and secondary vortex systems, for both examined angles of attack. The core structure of this third vortex, located between the secondary vortex and the wing leading edge, remained coherent and persisted from wing apex to the trailing edge. The BLE solutions with the SA turbulence model indicated a part span leading-edge flow separation and the associated upstream progression with increasing angle of attack. Unlike the solutions with the SA, the high angle-of-attack BLE results based on the BL/DS model indicated the existence of a weak bubble like flow separation around the apex region. The corresponding load distribution associated with

this separated bubble was verified with the experimental data. Furthermore, the BLE solution with the BL/DS model at high angle of attack showed a burst region occurring in primary vortex core near the trailing edge where the computed surface pressure coefficients agreed reasonably well with the data. Every solution, regardless of the different leading-edge geometry, angle of attack, turbulence model, and flux splitting scheme indicated the presence a separation line near and roughly parallel to the wing trailing edge.

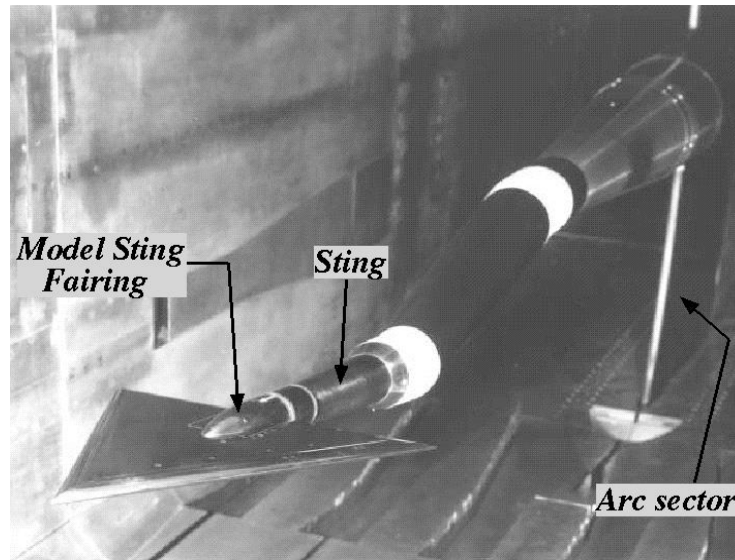
The challenges associated with the numerical simulation of the leading-edge flow separation and the ensuing vortical flow characteristics have been explored for the present delta wing. Within the scope of the present investigation and analysis, it can generally be concluded that the BL/DS turbulence model coupled with the fvs scheme provides the most effective combination for numerical simulation of the subject vortical flows over the present SLE configuration. Similarly, the SA turbulence model coupled with the fvs often yields the best combination for simulating the leading-edge flow separation and the off-surface vortical flows over the present BLE configuration. The results and the process requirements have demonstrated the viability of the present numerical method for predicting, with a reasonable degree of accuracy, the incremental aerodynamic load distributions for the present delta wing having either a sharp or blunt leading-edge geometry at the examined flow conditions.

References

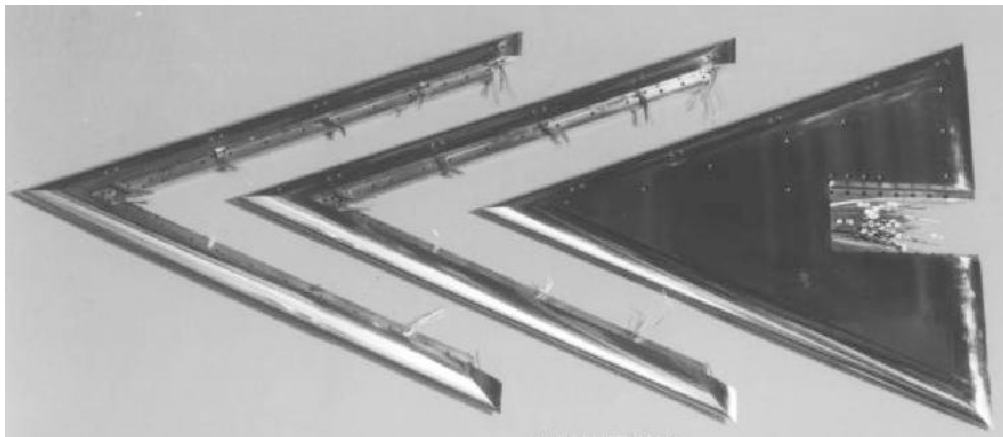
1. Hartwich, P. -M., and Hall, R. M.: Navier-Stokes Solutions for Vortical Flows over a Tangent-Ogive Cylinder. *AIAA Journal*, Vol. 28, No. 7, July 1990, pp. 1171-1179.
2. Thomas, J. L., Walters, R. W., Reu, T., Ghaffari, F., Weston, R. P., and Luckring, J. M.: Application of a Patched-Grid Algorithm to the F/A-18 Forebody-Leading-Edge Extension Configuration. *Journal of Aircraft*, vol. 27, No. 9, September 1990, pp. 479-456.
3. Ghaffari, F., Luckring, J. M., Thomas, J. L., and Bates, B. L.: Navier-Stokes Solutions

- About the F/A-18 Forebody-Leading-Edge Extension Configuration. *Journal of Aircraft*, vol. 27, No. 9, September 1990, pp. 737-748.
4. Mason, W. H., and Ravi, R.: Computational Study of the F-5A Forebody Emphasizing Directional Stability. *Journal of Aircraft*, Vol. 31, No. 3, May-June 1994, pp. 488-494.
 5. Hemsch, M. J., Jacobs, P. F., and Hall, R. M.: High-Angle-of-Attack Aerodynamic Characteristics and Surface Pressures for a Related Series of Advanced Slender Forebodies at Subsonic Speeds. NASA TP-3471, September 1994.
 6. Ravi, R., and Mason, W. H.: Chine-Shaped Forebody Effects on Directional Stability at High- α . *Journal of Aircraft*, Vol. 31, No. 3, May-June 1994, pp. 488-494.
 7. Ghaffari, F.: On the Vortical-Flow Prediction Capability of an Unstructured-Grid Euler Solver. AIAA Paper No. 94-0163, January 1994.
 8. Wilson, H. A. and Lovell, J. C.: Full-Scale Investigation of the Maximum Lift and Stability of an Airplane Having Approximately Triangular Plan Form. NACA RM No. L6K20, 1946.
 9. Hummel, D.: On the Vortex Formation over a Slender Wing at Large Angles of Incidence. AGARD-CP-247, Paper No. 15, January 1979.
 10. Chu, J., and Lamar, J. E.: Force and Pressure Study of Thick Cambered/Twisted 58 Deg. Delta Wings. *Journal of Aircraft*, Vol. 25, No. 1, January 1988, pp. 69-75.
 11. Roos, F., and Kegelmann, J.: An Experimental Investigation of Sweep-Angle Influence on Delta-Wing Flows. AIAA Paper No. 90-0383, 1990.
 12. Wood, N. J., Roberts, L., and Celik, Z.: Control of Asymmetric Vortical Flows over Delta Wings at High Angles of Attack. *Journal of Aircraft*, Vol. 27, No. 5, May 1990.
 13. Erickson, G. E., and Rogers, L. W.: Effects of Forebody Strakes and Mach Number on Overall Aerodynamic Characteristics of Configuration With 55° Cropped Delta Wing. NASA Technical Paper 3253, November 1992.
 14. Thomas, J. L., Newsome, R. W.: Navier-Stokes Computations of Lee-Side Flows Over Delta Wings. AIAA Paper No. 86-1049, May 1986.
 15. Thomas, J. L., Taylor, S. L., Anderson, W. K.: Navier-Stokes Computations of Vortical Flows Over Low Aspect Ratio Wings. AIAA Paper No. 87-0207, January 1987.
 16. Newsome, R. W., and Kandil, O. A.: Vortical Flow Aerodynamics – Physical Aspects and Numerical Simulation. AIAA Paper No. 87-0205, January 1987.
 17. Hoeijmakers, H. W. M.: Modeling and Numerical Simulation of Vortex Flow in Aerodynamics. AGARD-CP-494, Paper No. 1, October 1-4, 1990.
 18. Gordnier, R. E.: Computational Study of a Turbulent Delta-Wing flowfield Using Two-Equation Turbulence Models. AIAA Paper No. 96-2076, June 1996.
 19. Murman, S. M., and Chaderjian, N. M.: Application of Turbulence models to separated High-Angle-of-Attack Flows. AIAA Paper No. 98-4519, 1998.
 20. Görtz, S., Rizzi, A.: Computing the High-Alpha Aerodynamics of Delta Wings – Evaluation and Analysis. AIAA Paper No. 01-0115, January 2001.
 21. Morton, S. A., Forsythe, J. R., Mitchell, A. M., and Hajek, D.: DES and RANS Simulations of Delta Wing Vortical Flows. AIAA Paper No. 2002-0587, January 2002.
 22. Chu, J., and Luckring, J. M.: Experimental Surface Pressure Data Obtained on a 65° Delta Wing Across Reynolds Number and Mach Number Ranges. Volume 1 – Sharp Leading Edge. NASA TM-4645, February 1996.
 23. Chu, J., and Luckring, J. M.: Experimental Surface Pressure Data Obtained on a 65° Delta Wing Across Reynolds Number and Mach Number Ranges. Volume 2 – Small Leading Edge. NASA TM-4645, February 1996.
 24. Chu, J., and Luckring, J. M.: Experimental Surface Pressure Data Obtained on a 65° Delta Wing Across Reynolds Number and Mach Number Ranges. Volume 3 – Medium Leading Edge. NASA TM-4645, February 1996.
 25. Chu, J., and Luckring, J. M.: Experimental Surface Pressure Data Obtained on a 65° Delta Wing Across Reynolds Number and Mach Number Ranges. Volume 4 – Large Leading Edge. NASA TM-4645, February 1996.
 26. Luckring, J. M.: Reynolds Number and Leading-Edge Bluntness Effects on a 65° Delta

- Wing. AIAA Paper No. 2002-0419, January 2002.
27. Luckring, J. M.: Transonic Reynolds Number and Leading-Edge Bluntness Effects on a 65° Delta Wing. AIAA Paper No. 2003-0753, January 2003.
 28. Luckring, J. M.: Compressibility and Leading-Edge Bluntness Effects for a 65° Delta Wing. AIAA Paper No. 2004-0765, January 2004.
 29. Luckring, J. M.: Reynolds Number, Compressibility, and Leading-Edge Bluntness Effects on Delta Wing Aerodynamics. *24th Congress on the International Council of Sciences (ICAS)*, Yokohama, Japan, August 29- September 3, 2004.
 30. Londenberg, W. K.: Transonic Navier-Stokes Calculations About a 65° Delta Wing. NASA CR-4635, November 1994.
 31. Pirzadeh, S. Z.: Vortical Flow Prediction Using an Adaptive unstructured Grid Method. NATO/RTO Applied Vehicle Technology Panel Symposium an Advanced Flow Measurement: Vortex Flow and High Angle of Attack, Paper No. 13, Loen Norway, May 7-10, 2001.
 32. Wahls, R. A.: The National Transonic Facility- A Research Retrospective. AIAA Paper No. 2001-0754, January 2001.
 33. Krist, S. L., Biedron, R. T., and Rumsey, C. L.: CFL3D User's Manual (Version 5.0), NASA TM-1998-208444, June 1998.
 34. Roe, P. L.: Characteristic-Based Schemes for the Euler Equations. *Annual Review of Fluid Mechanics*, Volume 18, Milton van Dyke, J. V. Wehausen, and John L. Lumley, Eds. Annual Reviews Inc., 1986, pp. 337-365.
 35. van Leer, Bram: Upwind-Difference Methods for Aerodynamic Problems Governed by the Euler Equations. *Large-scale Computations in Fluid Mechanics*, Bjorn E. Engquist, Stanely Osher, and Richard C.J. Somerville, eds. American Math. Soc., 1985, pp. 327-336.
 36. Biedron, R. T., Thomas, J. L.: A Generalized Patched-Grid Algorithm With Application to the F-18 Forebody With Actuated Control Strake. *Comput. Sys. Eng.*, Vol. 1, nos. 2-4, 1990, pp. 563-576.
 37. Baldwin, B. S., and Lomax, H.: Thin Layer Approximation and Algebraic Model for Separated Turbulent Flows. AIAA Paper No. 78-0257, January 1978.
 38. Degani, D., and Schiff, L. B.: Computation of Supersonic Viscous Flows Around Pointed Bodies at Large Incidence. AIAA Paper No. 83-0034, January 1983.
 39. Spalart, P. R., Allmaras, S. R.: A One-Equation Turbulence Model for Aerodynamic Flows. *La Recherche Aerospatiale*, No. 1, 1994, pp. 5-21.
 40. Dol, H. S., Kok, J. C., Oskam, B.: Turbulence Modelling for Leading-Edge Vortex Flows. AIAA Paper No. 2002-0843, January 2002.
 41. Gatski, T. B.: Turbulence Modelling for Aeronautical Flows. VKI Lecture Series, CFD-Based Aircraft Drag Prediction and Reduction, 3-7 November 2003.



(a) – Delta wing model installed in the NTF.



(b) – Delta wing model with three of the leading-edge components.

Figure 1 . Delta wing model installed in the tunnel and its components (Ref. 22).

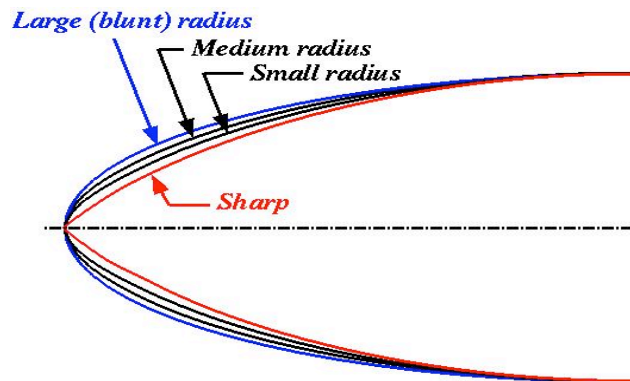


Figure 2. Schematic representation of the four different leading-edge contours.

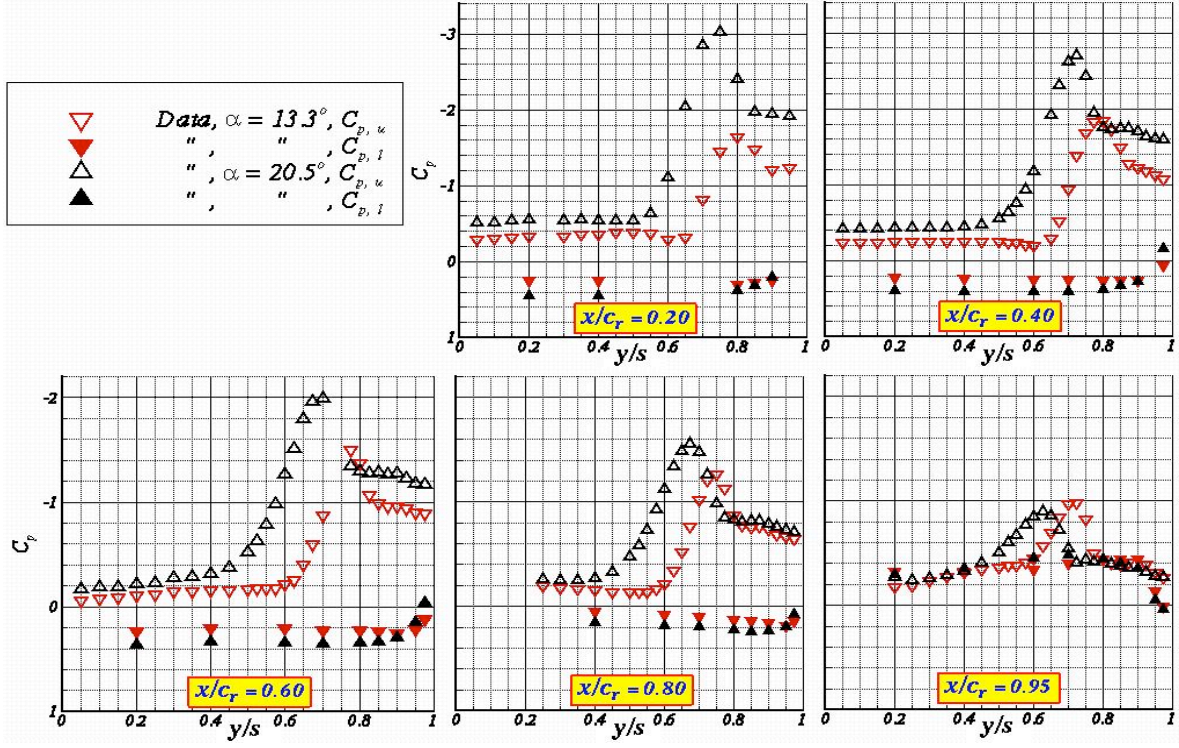


Figure 3. Effect of angle-of-attack on the measured surface C_p for the SLE at $M_\infty=0.40$, $R_\infty=6 \times 10^6$ (Data from Ref. 22).

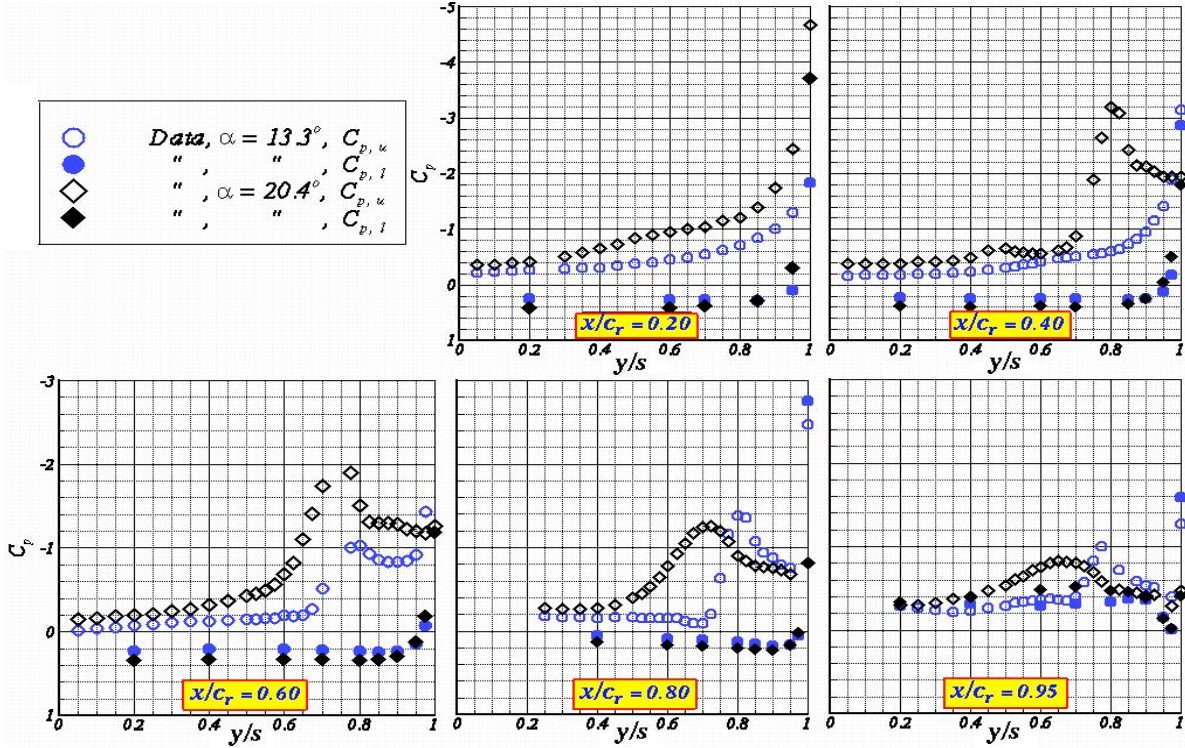


Figure 4. Effect of angle-of-attack on the measured surface C_p for the BLE at $M_\infty=0.40$, $R_\infty=6 \times 10^6$ (Data from Ref. 25).

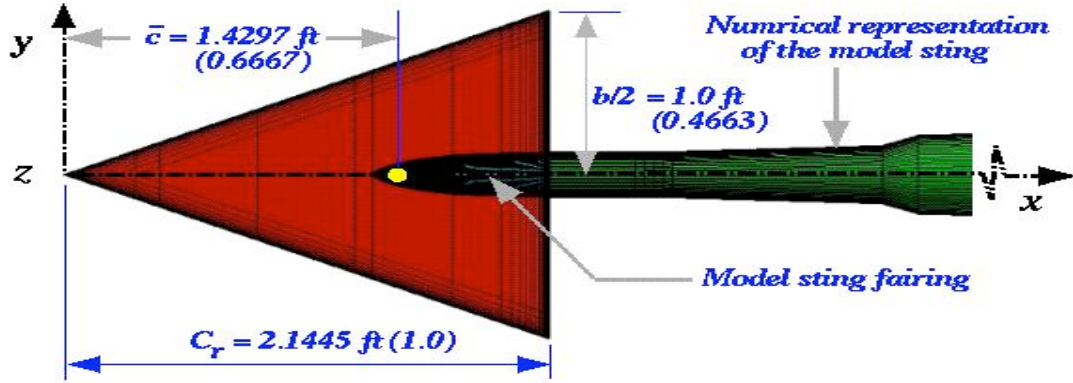


Figure 5. Planform view of the initial wire-frame definition for the numerical model (dimensions normalized by c_r are shown in parentheses).

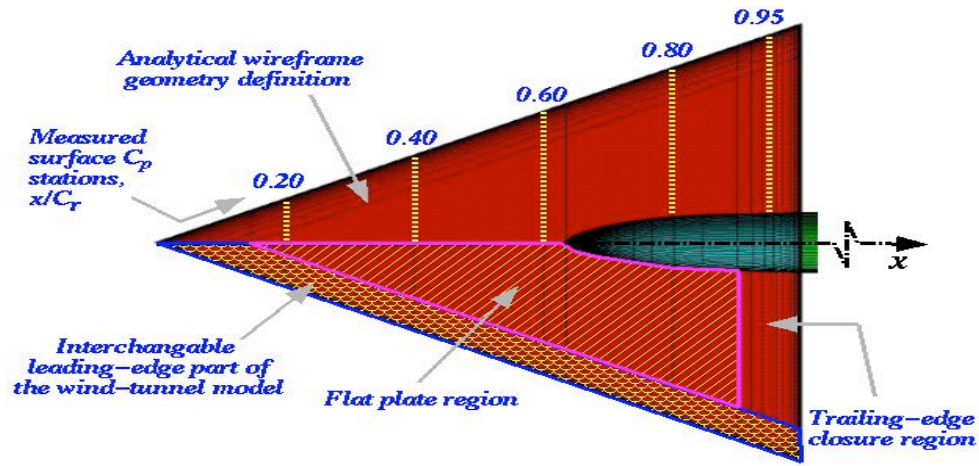


Figure 6. Planform view of the numerical model wire-frame geometry definition and its components.

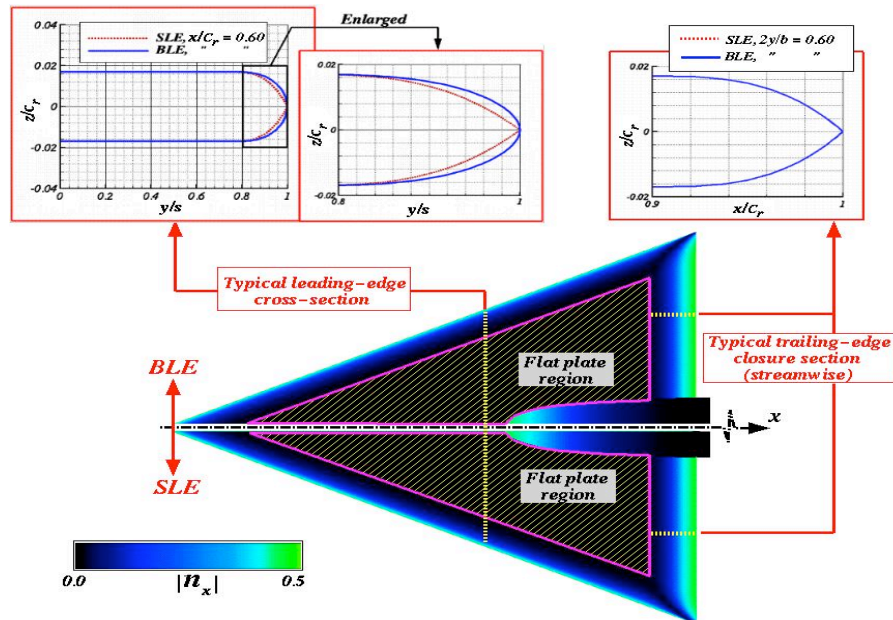


Figure 7. Surface unit-normal (x-component) variation of wire-frame geometry and typical sections.

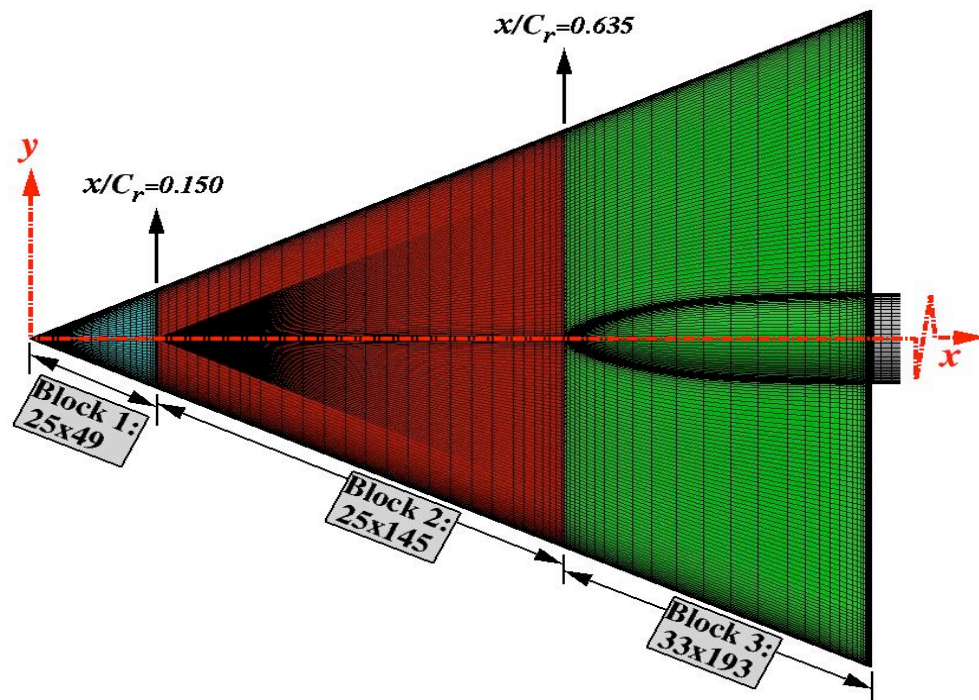


Figure 8. Top view of the SLE1 surface grid distribution.

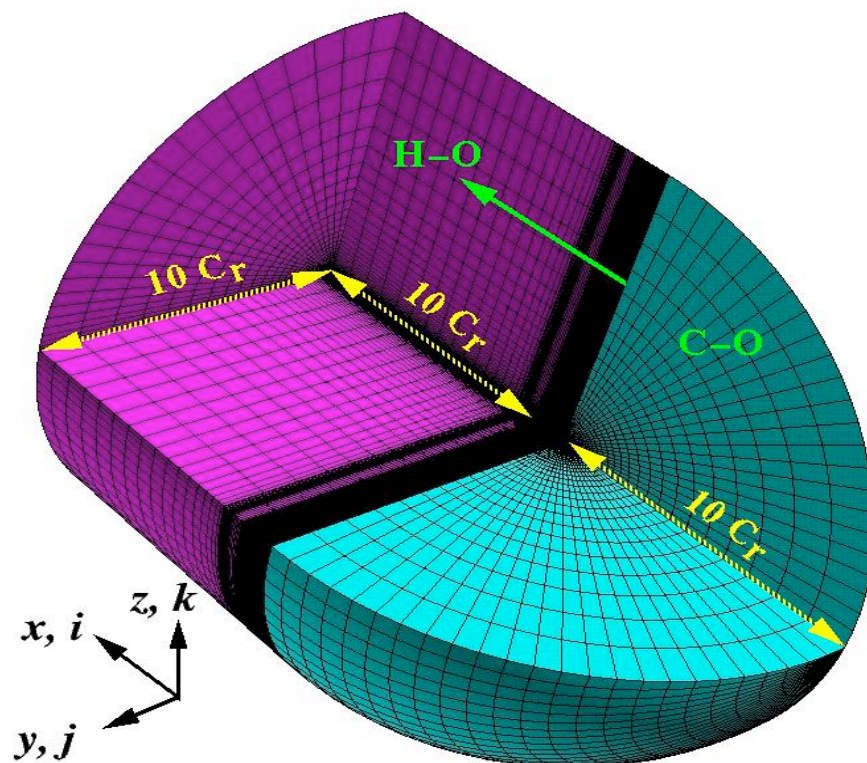


Figure 9. Typical far-field view of the overall volume grid topology.

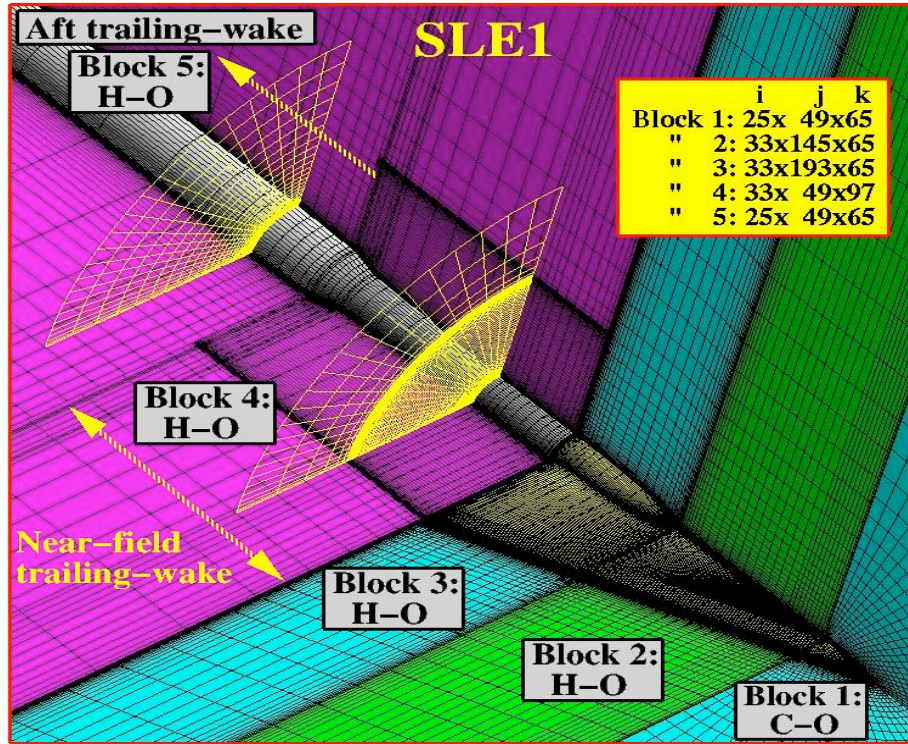


Figure 10. Oblique near-field view of the SLE1 grid topology.

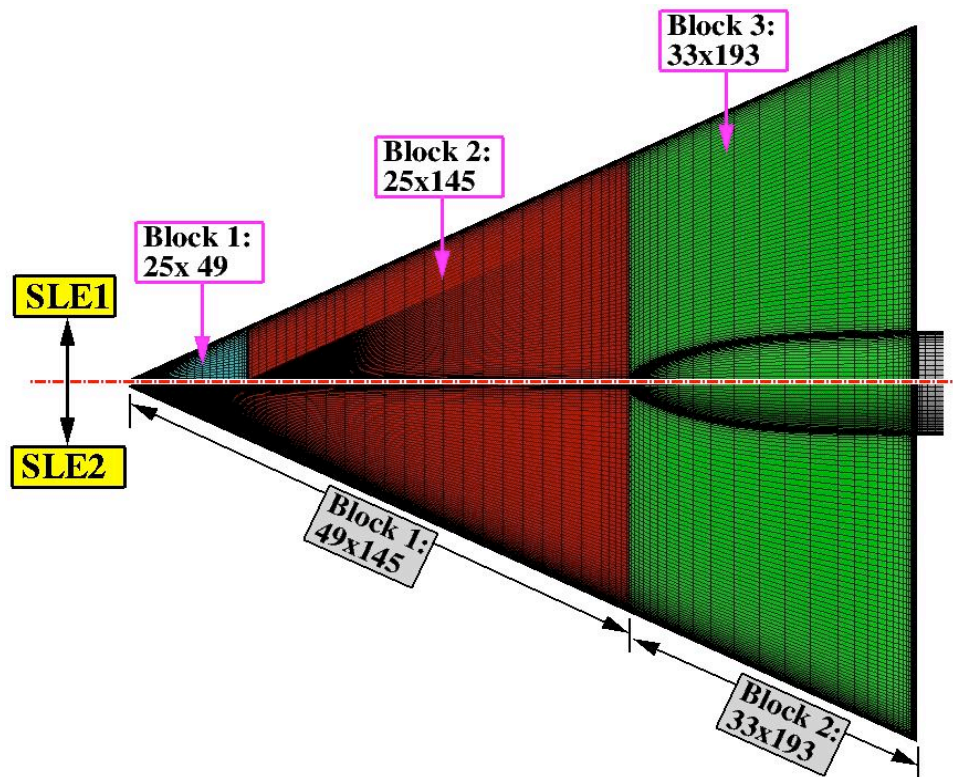


Figure 11. Top-view of the SLE1 and SLE2 surface grid distribution.

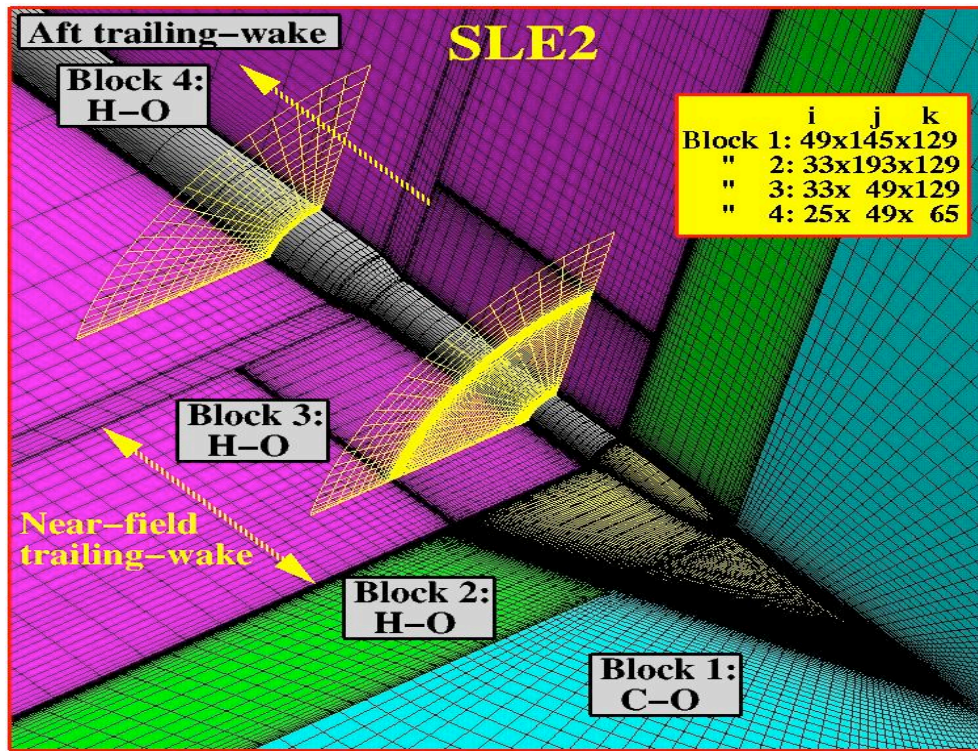


Figure 12. Oblique near-field view of the SLE2 grid topology.

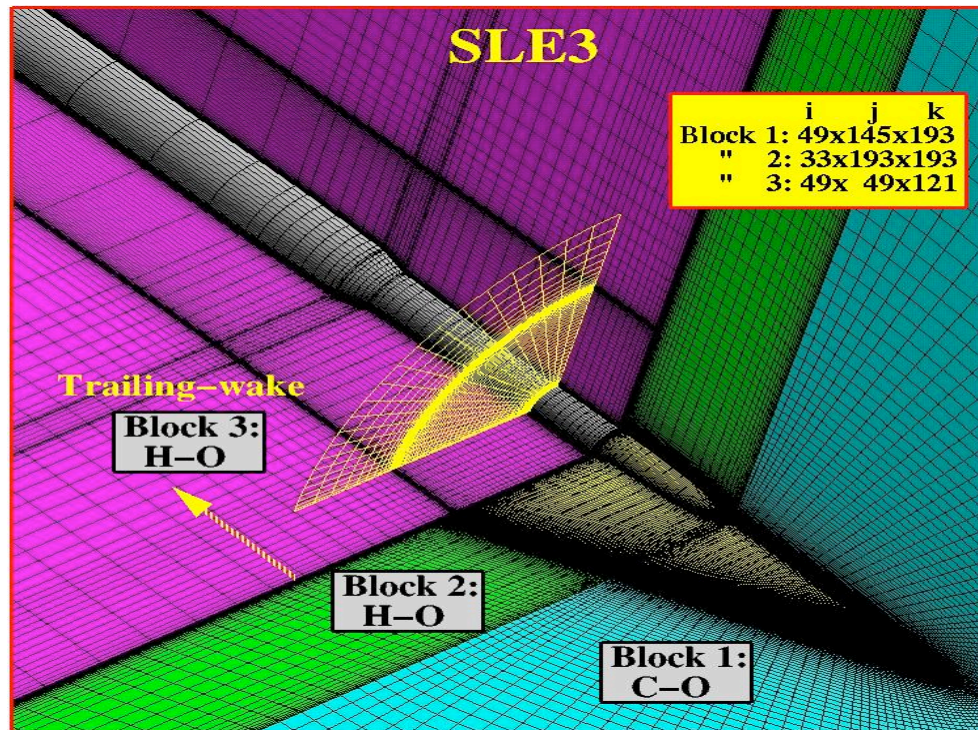


Figure 13. Oblique near-field view of the SLE3 grid topology.

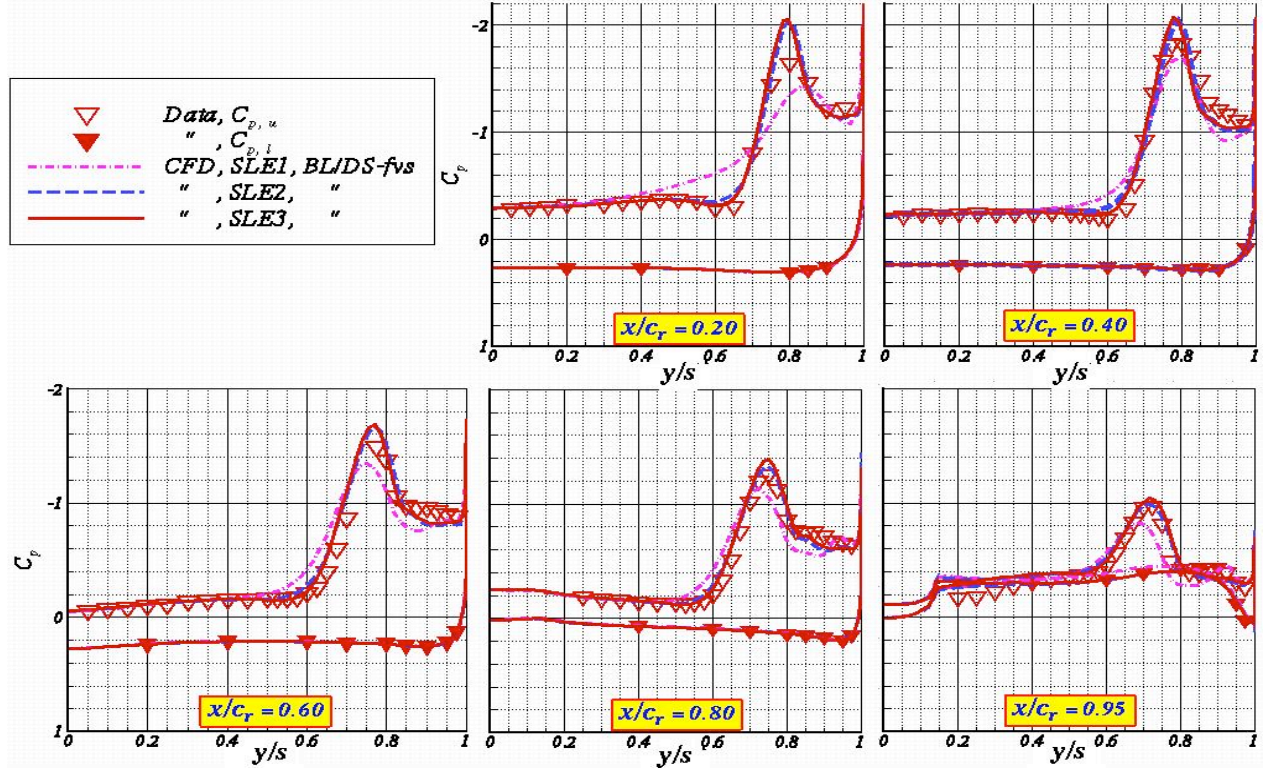


Figure 14. Grid sensitivity effects on the SLE computed C_p and correlation with data at $\alpha=13.3^\circ$, $M_\infty=0.40$, $R_\infty=6 \times 10^6$.

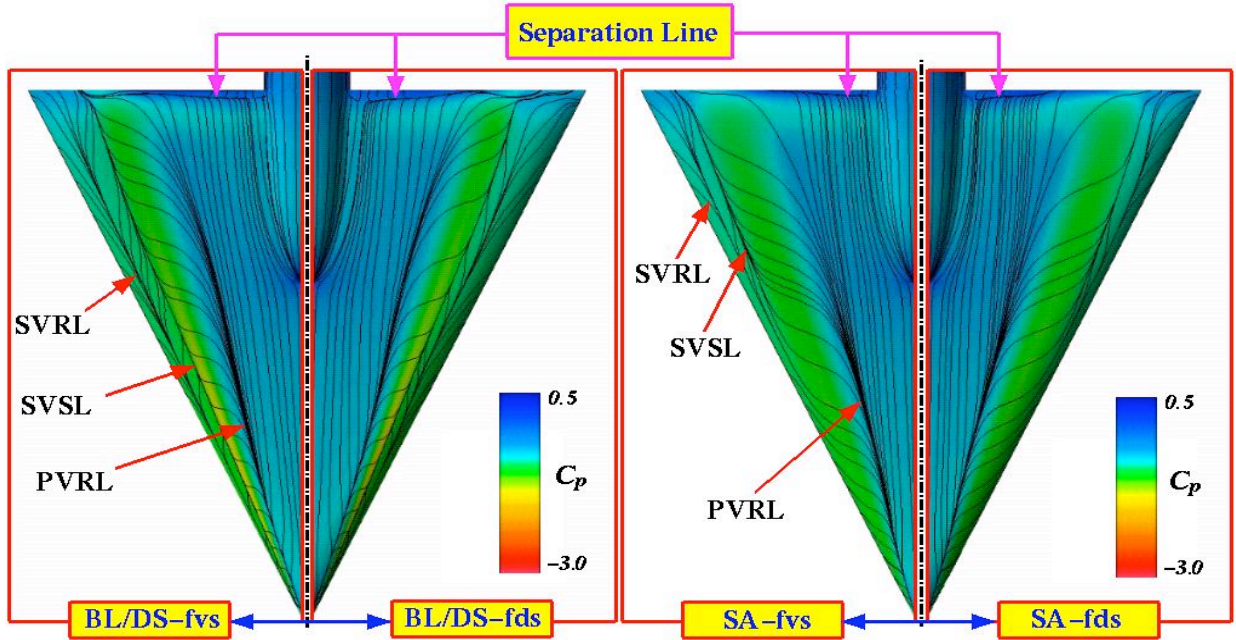


Figure 15. Turbulence model and flux splitting effects on computed surface flow features using the SLE3 grid at $\alpha=13.3^\circ$, $M_\infty=0.40$, $R_\infty=6 \times 10^6$.

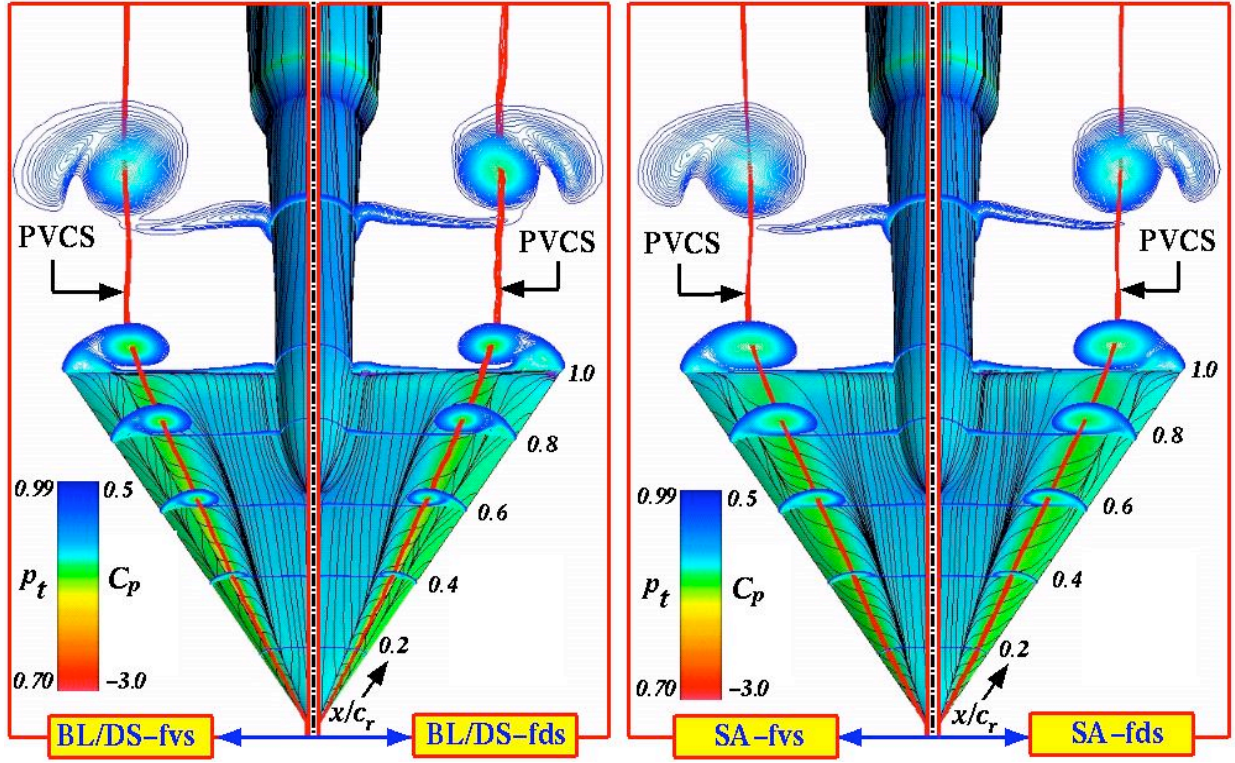


Figure 16. Turbulence model and flux splitting effects on computed on/off-surface flow features using the SLE3 grid at $\alpha=13.3^\circ$, $M_\infty=0.40$, $R_c=6 \times 10^6$.

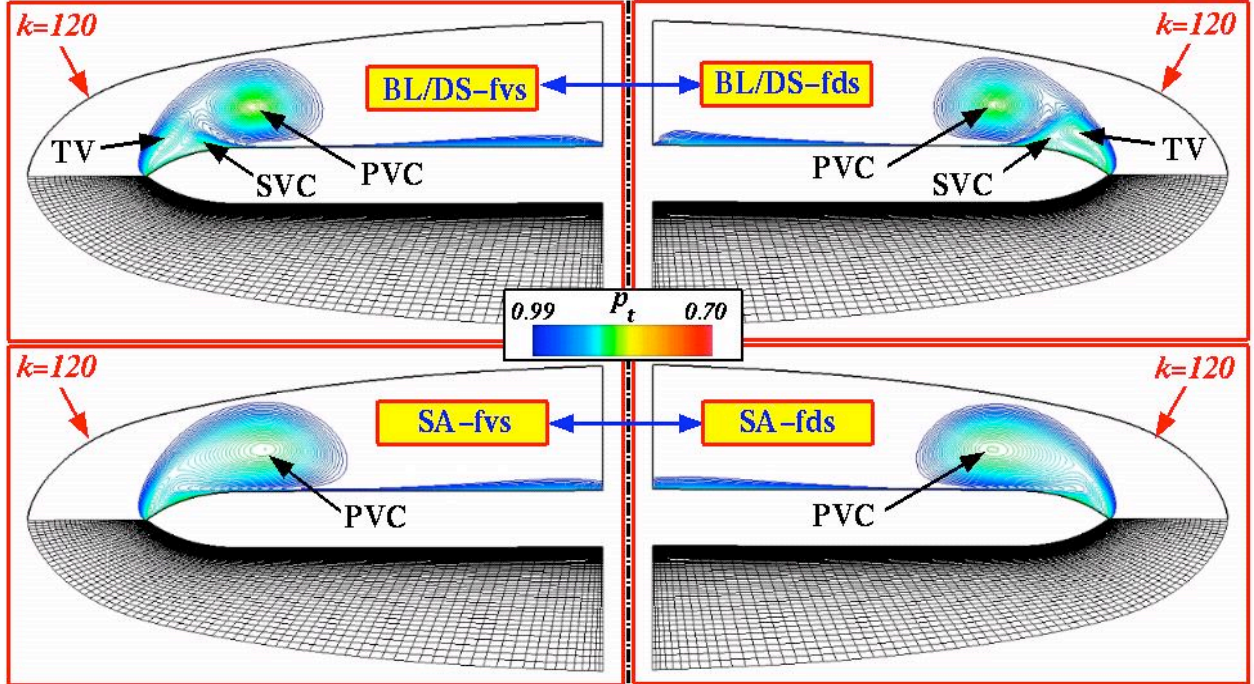


Figure 17. Turbulence model and flux splitting effects on computed cross-flow P_t using the SLE3 grid at $x/c_r=0.60$, $\alpha=13.3^\circ$, $M_\infty=0.40$, $R_c=6 \times 10^6$.

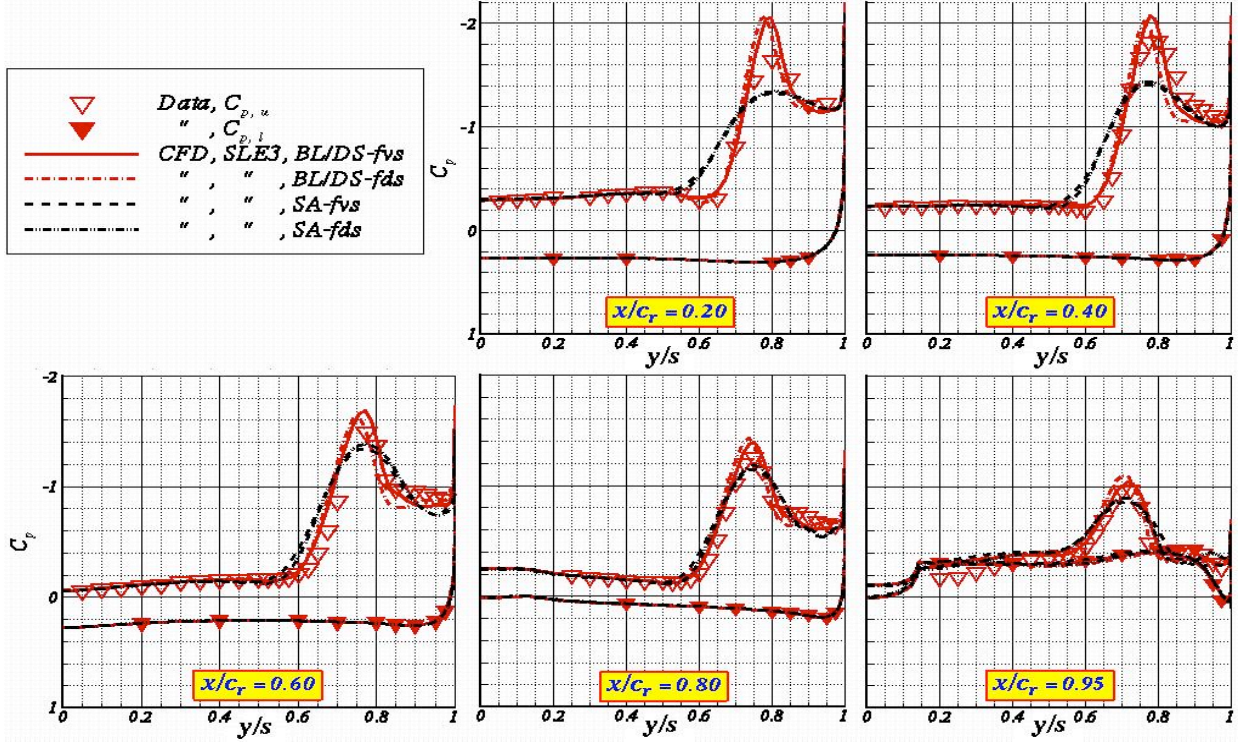


Figure 18. Turbulence model and flux splitting effects on the SLE computed C_p and correlation with data at $\alpha=13.3^\circ$, $M_\infty=0.40$, $Re=6 \times 10^6$.

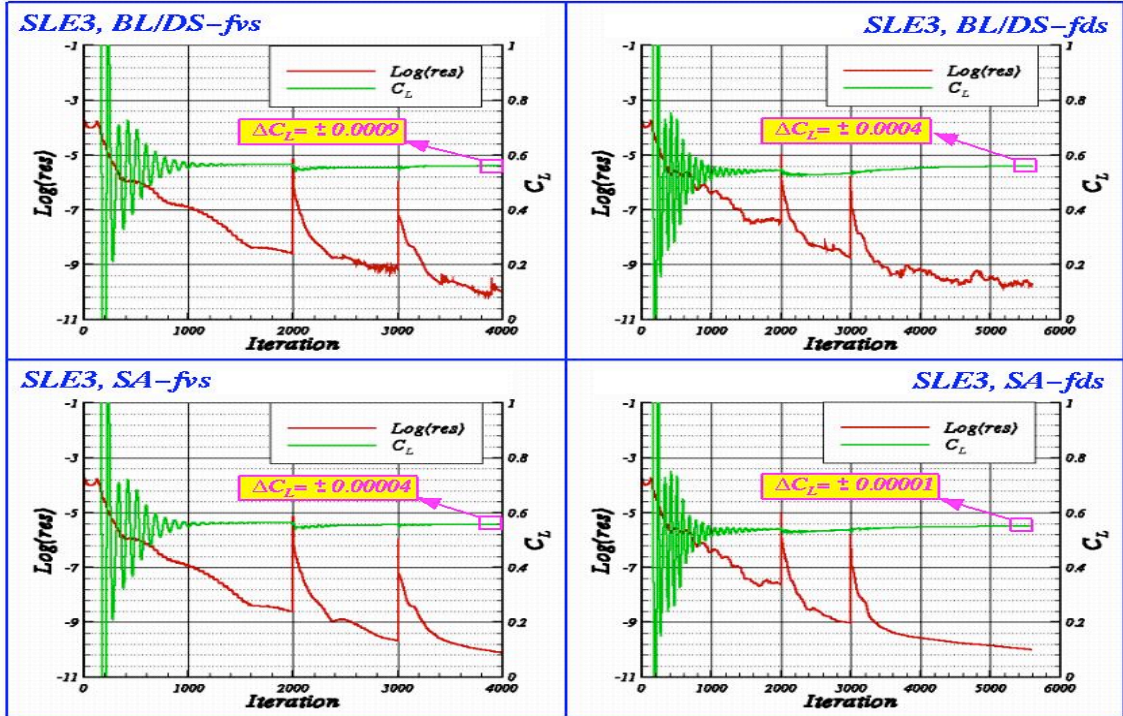


Figure 19. Turbulence model and flux splitting effects on the SLE solution convergence history at $\alpha=13.3^\circ$, $M_\infty=0.40$, $Re=6 \times 10^6$.

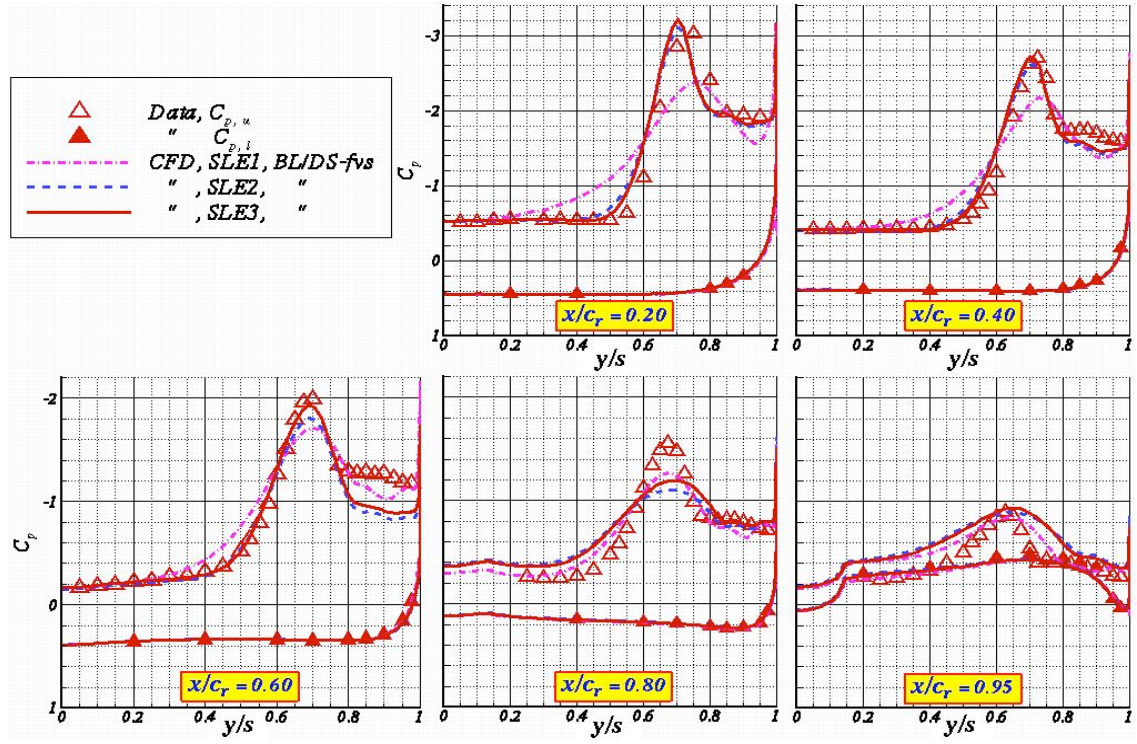


Figure 20. Grid sensitivity effects on the SLE computed C_p and correlation with data at $\alpha=20.5^\circ$, $M_\infty=0.40$, $Re=6 \times 10^6$.

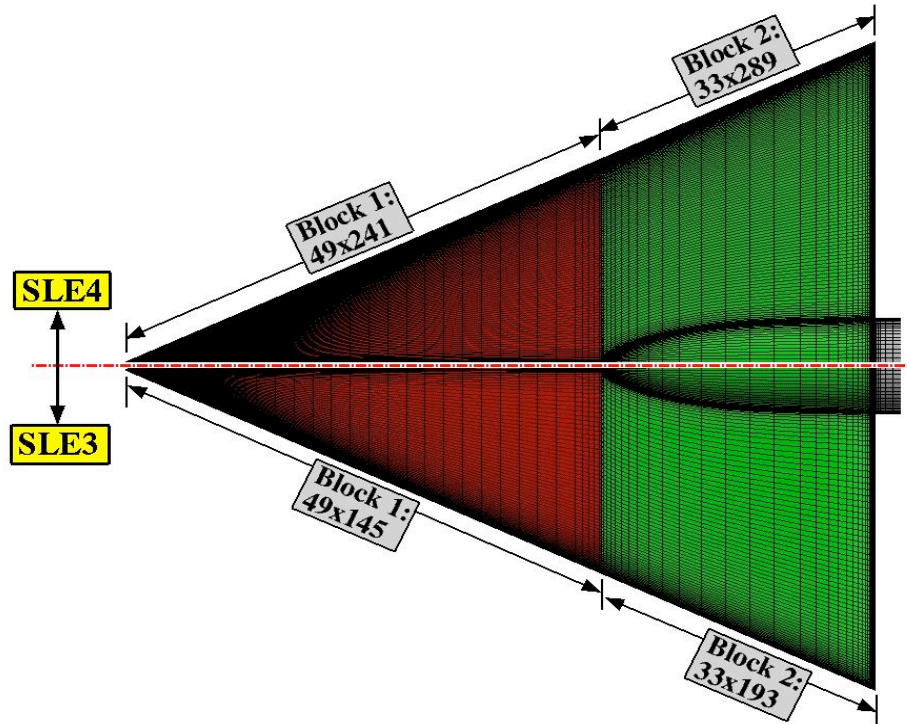


Figure 21. Planform view of the SLE4 surface grid distribution and comparison with the SLE3 grids.

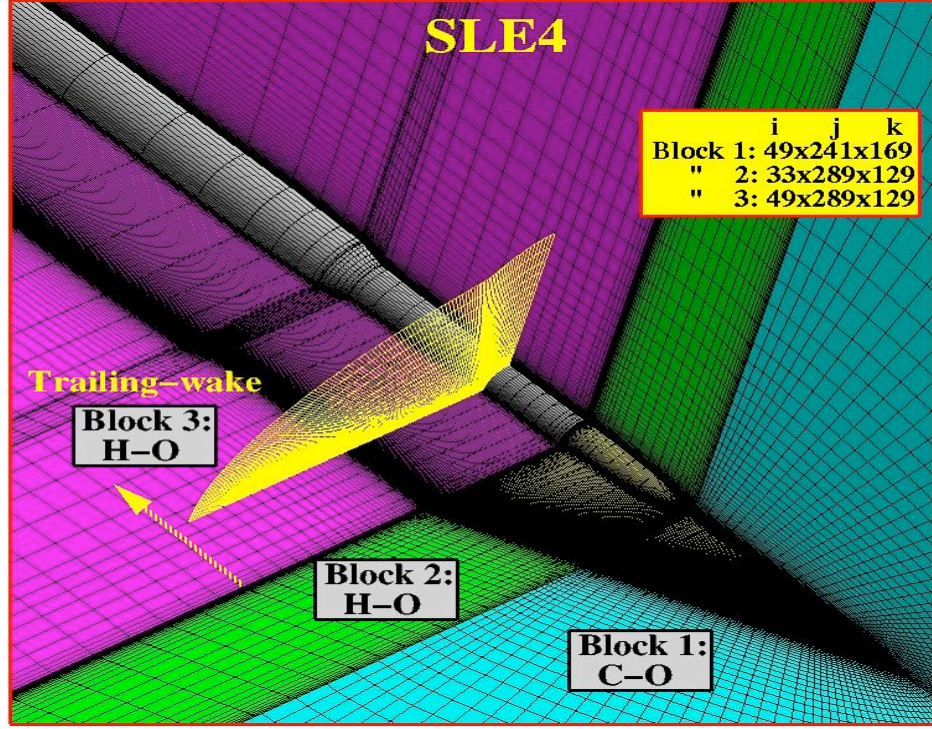


Figure 22. Oblique near-field view of the SLE4 volume grid topology.

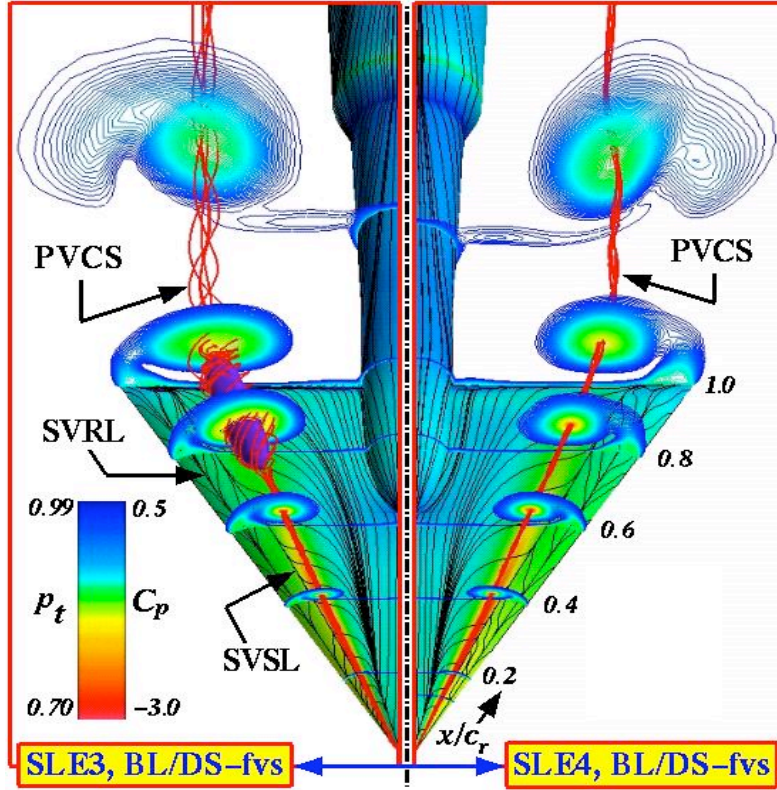


Figure 23. Effects of grid modifications on the SLE computed flow features at $\alpha=20.5^\circ$, $M_\infty=0.40$, $R_\infty=6 \times 10^6$.

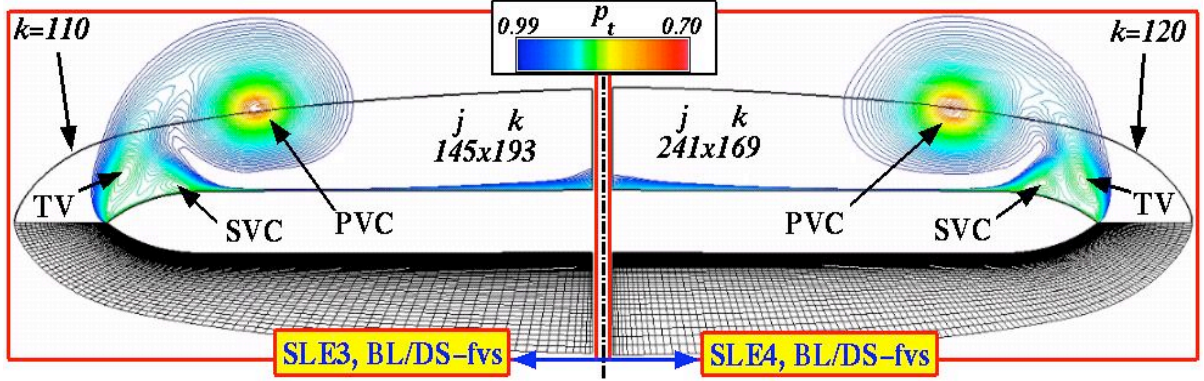


Figure 24. Effects of grid modifications on the SLE computed cross-flow p_t at $\alpha=20.5^\circ$, $M_\infty=0.40$, $R_c=6 \times 10^6$, $x/c_r=0.60$.

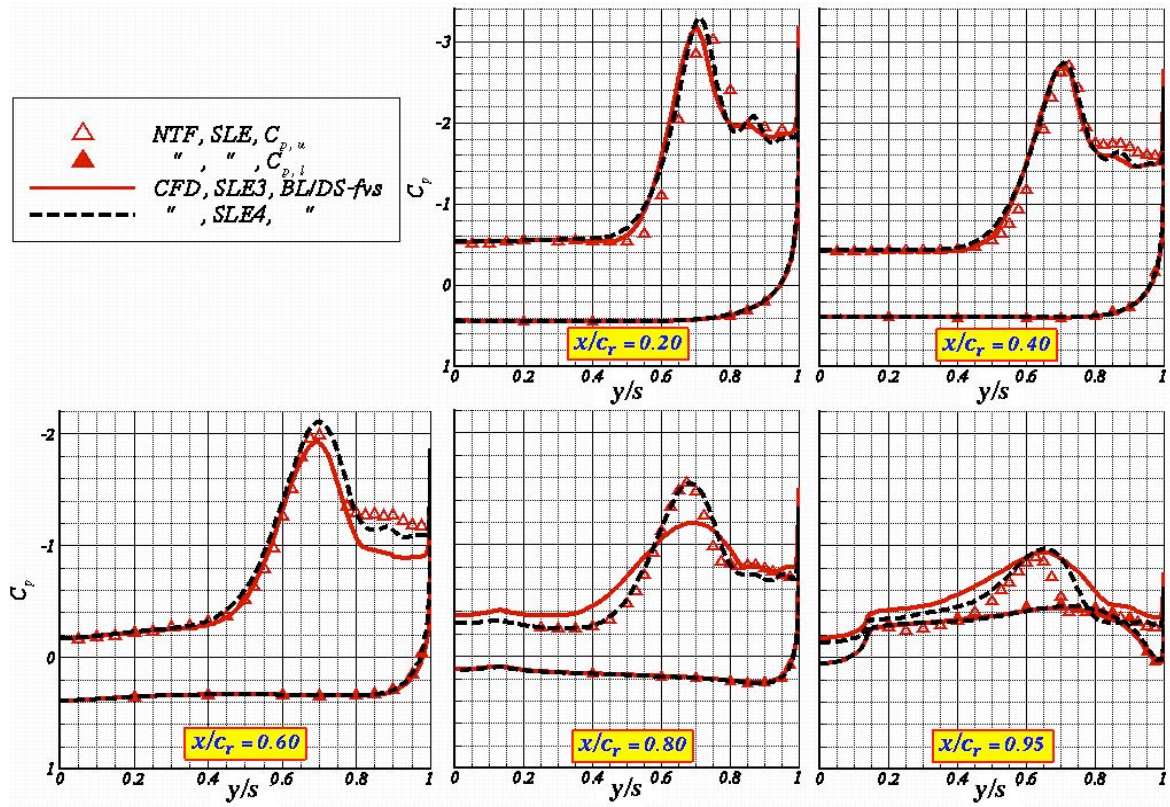


Figure 25. Effects of grid modifications on the SLE computed C_p and correlation with data at $\alpha=20.5^\circ$, $M_\infty=0.40$, $R_c=6 \times 10^6$.

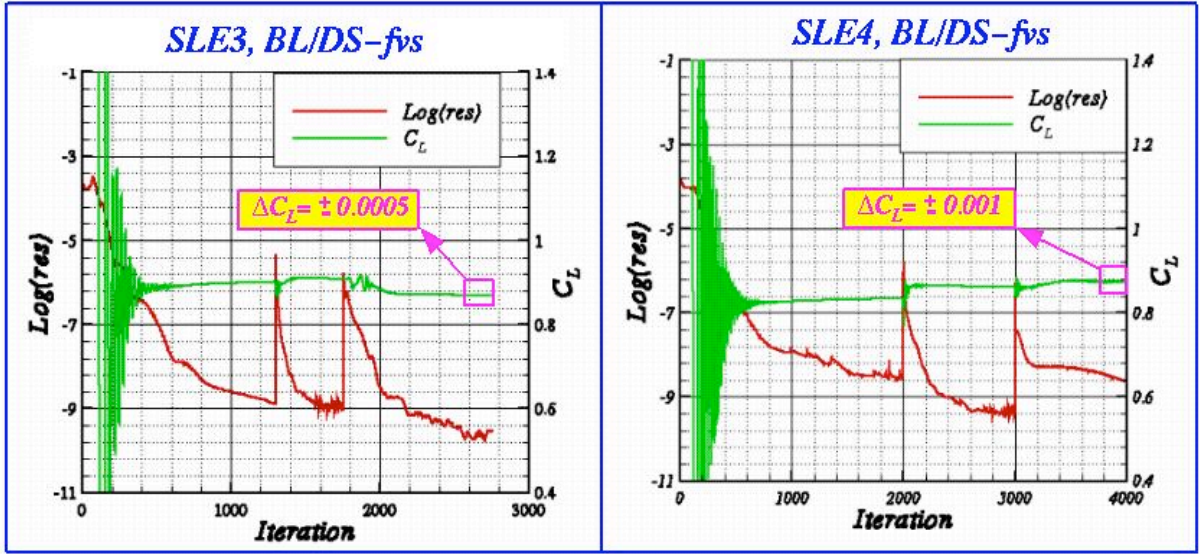


Figure 26. Effects of grid modifications on the SLE solution convergence at $\alpha=20.5^\circ$, $M_\infty=0.40$, $R_c=6 \times 10^6$.

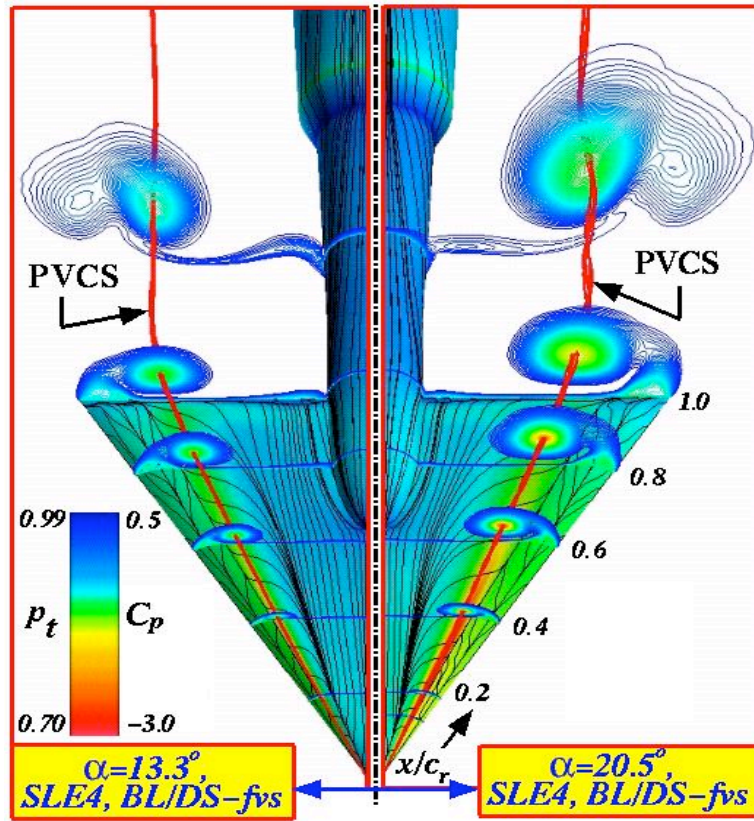


Figure 27. Effect of angle-of-attack on the computed SLE flow features at $M_\infty=0.40$, $R_c=6 \times 10^6$.

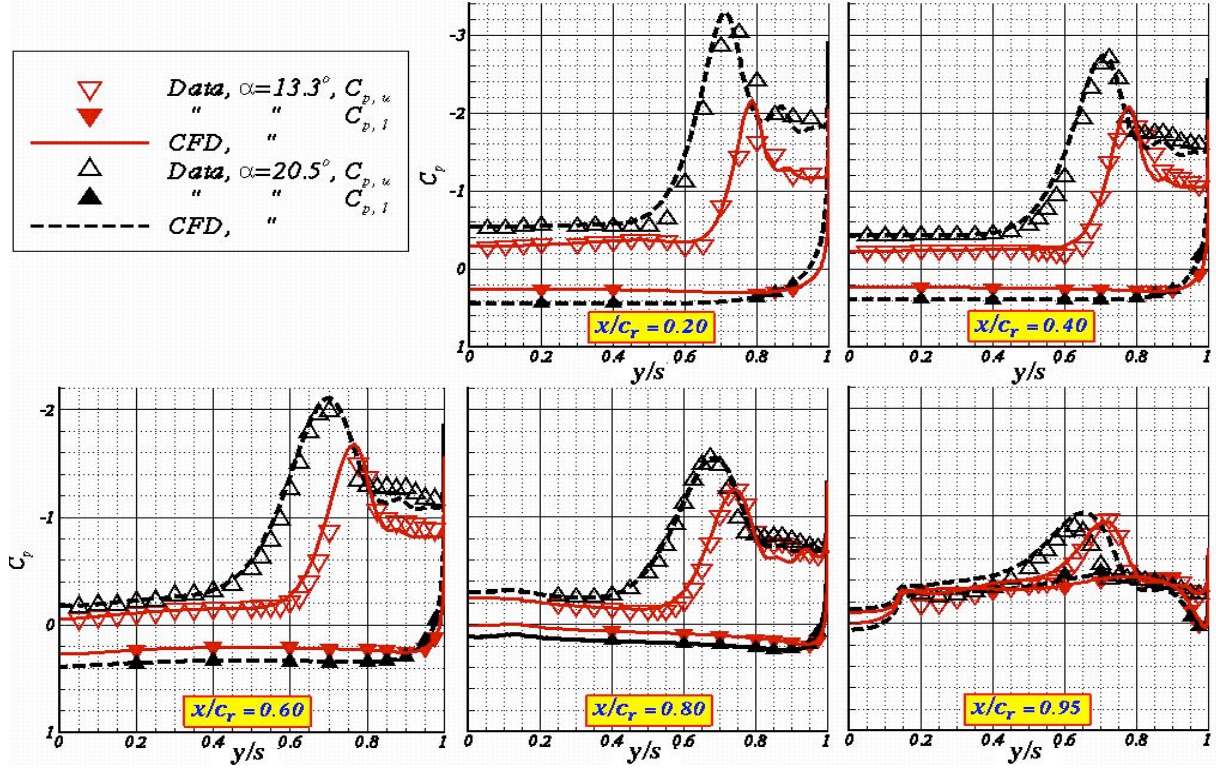


Figure 28. Effect of angle of attack on the SLE computed C_p and correlation with data at $M_\infty=0.40$, $Re=6 \times 10^6$.

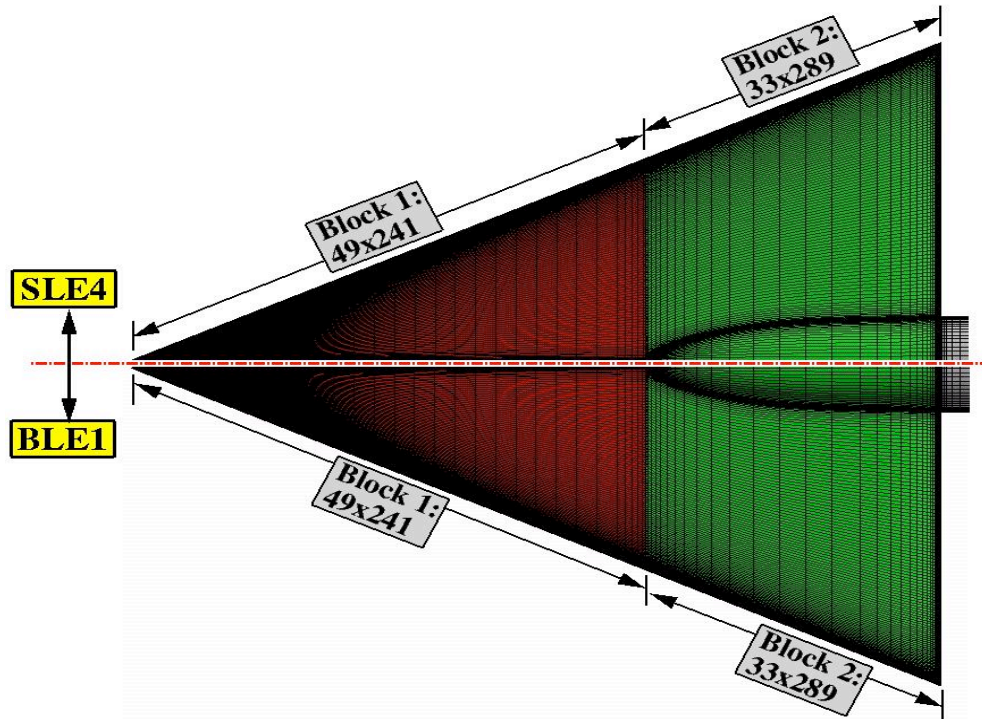


Figure 29. Computational surface grid for the BLE1 and comparison with the SLE4.

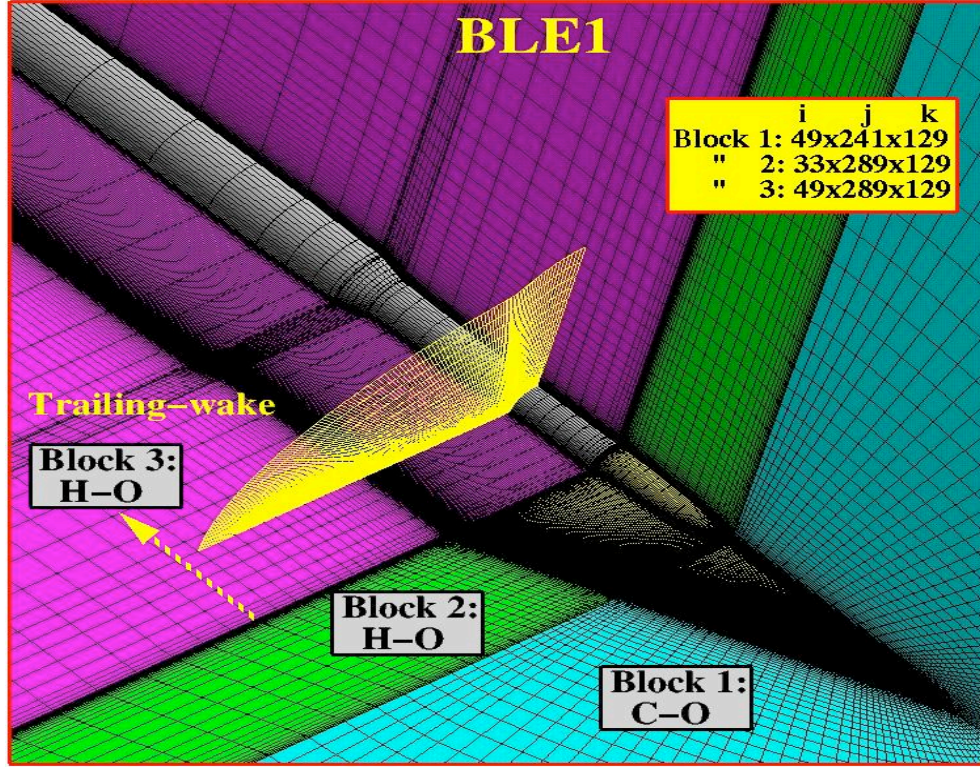


Figure 30. Oblique near-field view of the BLE1 grid topology.

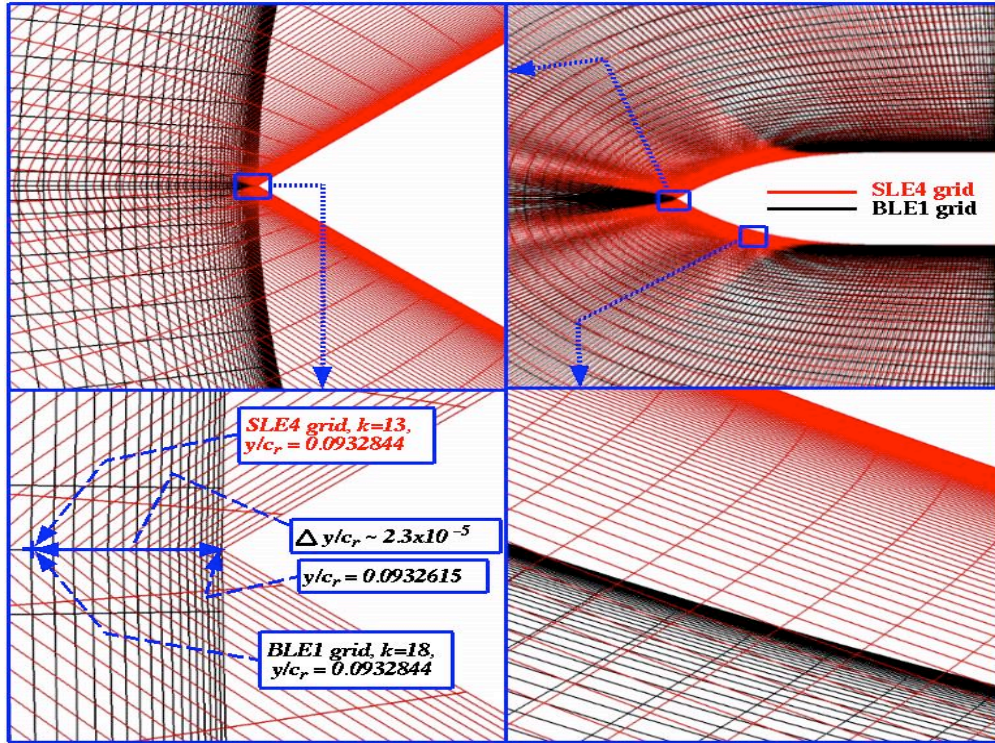


Figure 31. Typical cross-sectional grid comparison between the SLE4 and BLE1 grid strategies at $x/c_r=0.20$.

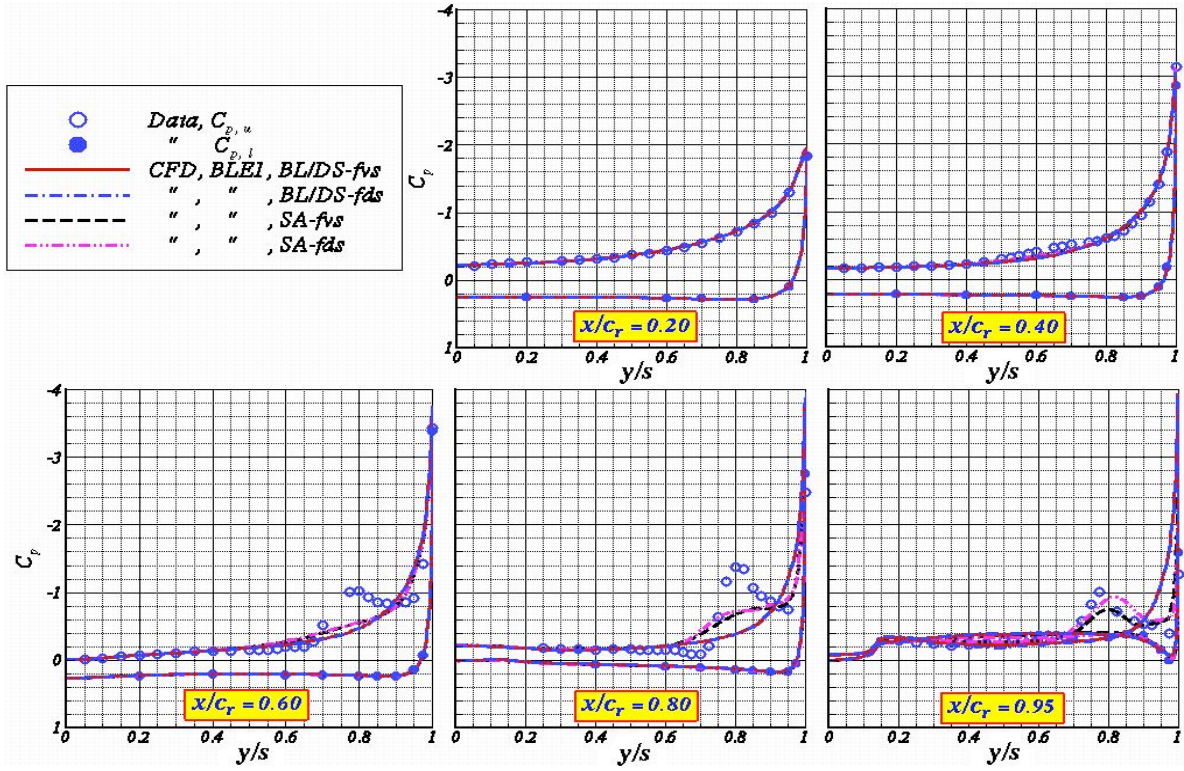


Figure 32. Turbulence model and flux splitting effects on the BLE computed C_p and correlation with data at $\alpha=13.3^\circ$, $M_\infty=0.40$, $R_\infty=6 \times 10^6$.

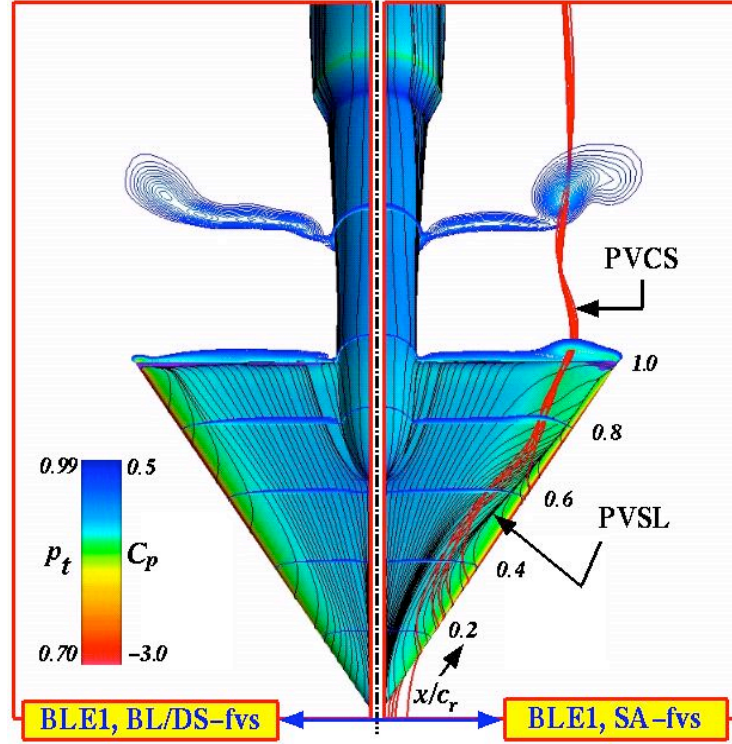


Figure 33. Effects of turbulence model on computed flow features using the BLE1 grid at $\alpha=13.3^\circ$, $M_\infty=0.40$, $R_\infty=6 \times 10^6$.

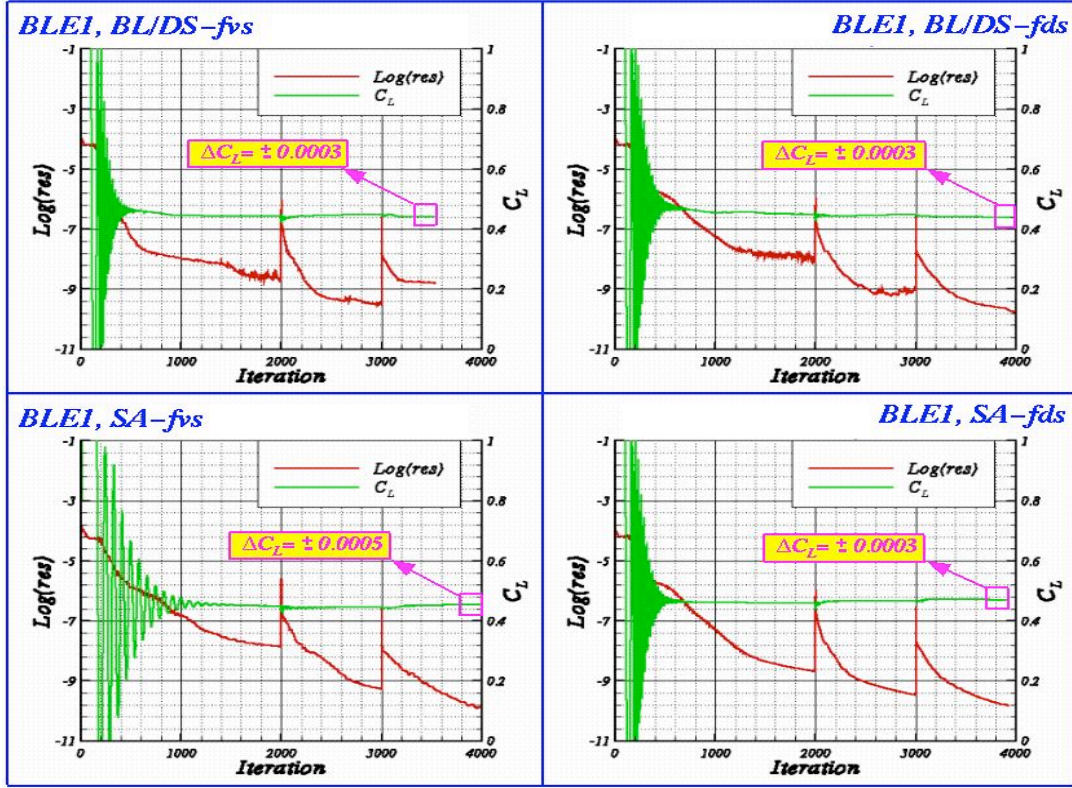


Figure 34. Turbulence model and flux splitting effects on BLE solution convergence history at $\alpha=13.3^\circ$, $M_\infty=0.40$, $R_\tau=6 \times 10^6$.

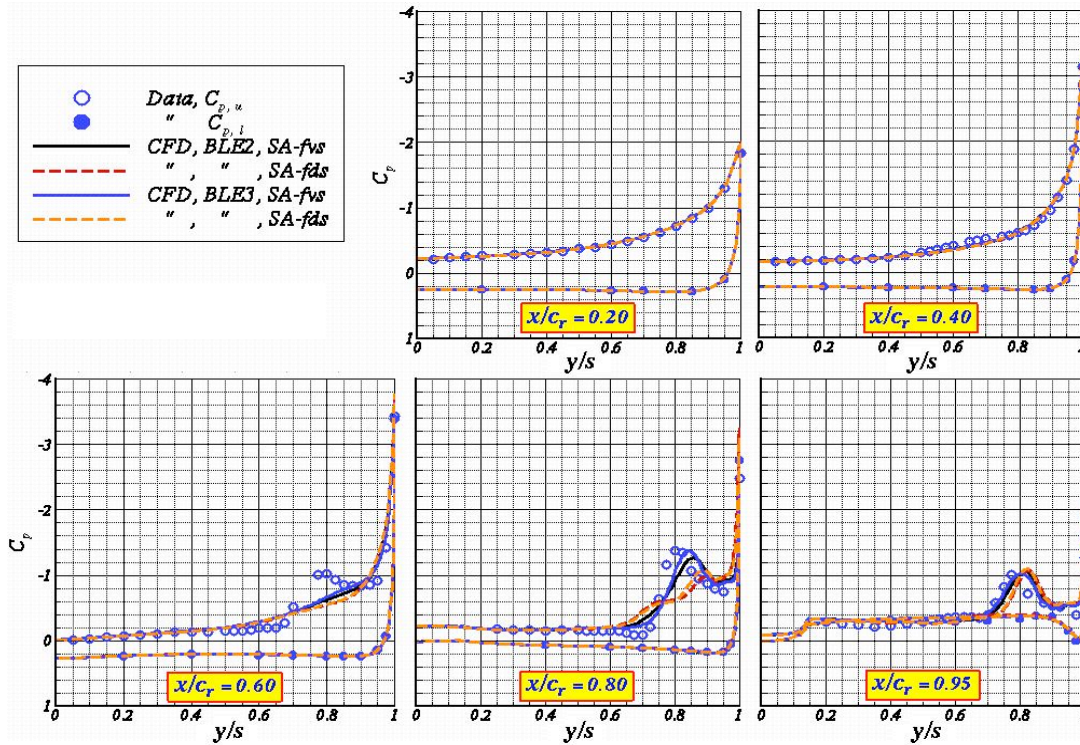


Figure 35. Grid sensitivity and flux splitting effects on the BLE computed C_p and correlation with data at $\alpha=13.3^\circ$, $M_\infty=0.40$, $R_\tau=6 \times 10^6$.

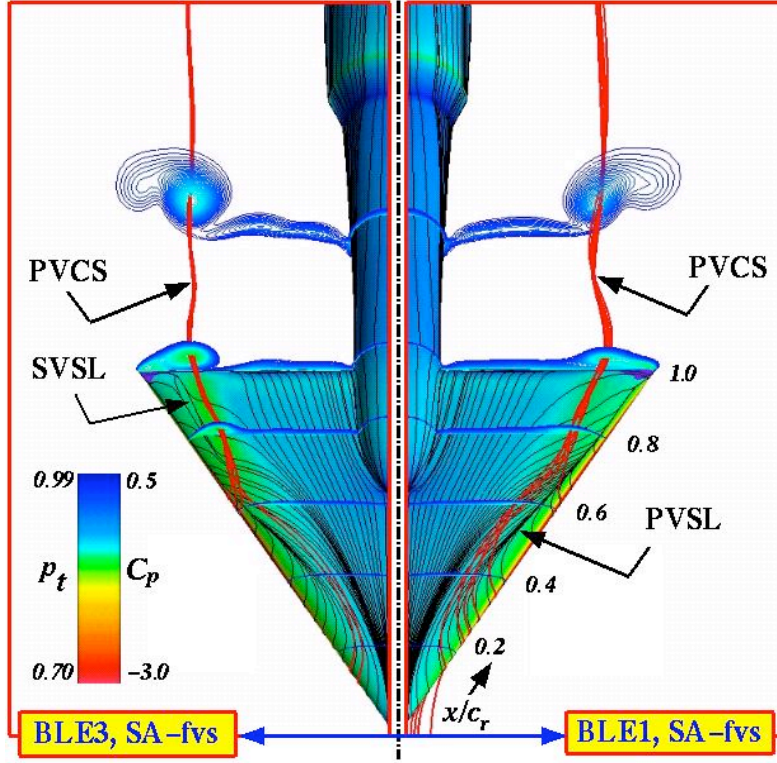


Figure 36. Effects of grid modifications on the BLE computed flow features at $\alpha=13.3^\circ$, $M_\infty=0.40$, $R_\infty=6 \times 10^6$.

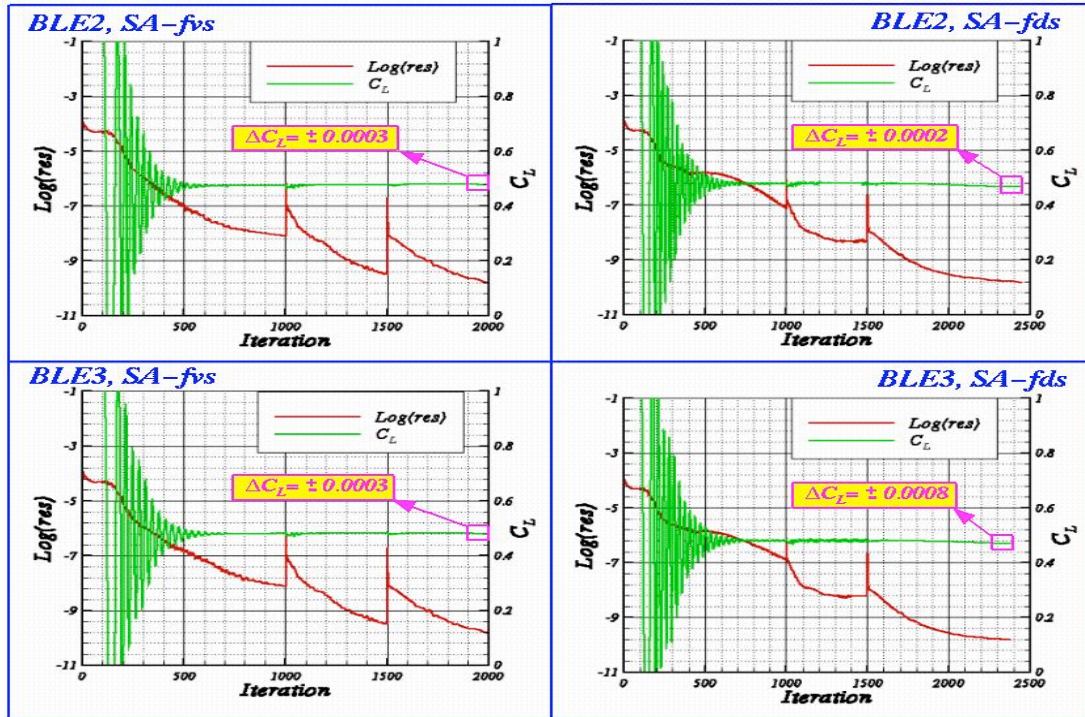


Figure 37. Grid sensitivity and flux splitting effects for the BLE solution convergence history at $\alpha=13.3^\circ$, $M_\infty=0.40$, $R_\infty=6 \times 10^6$.

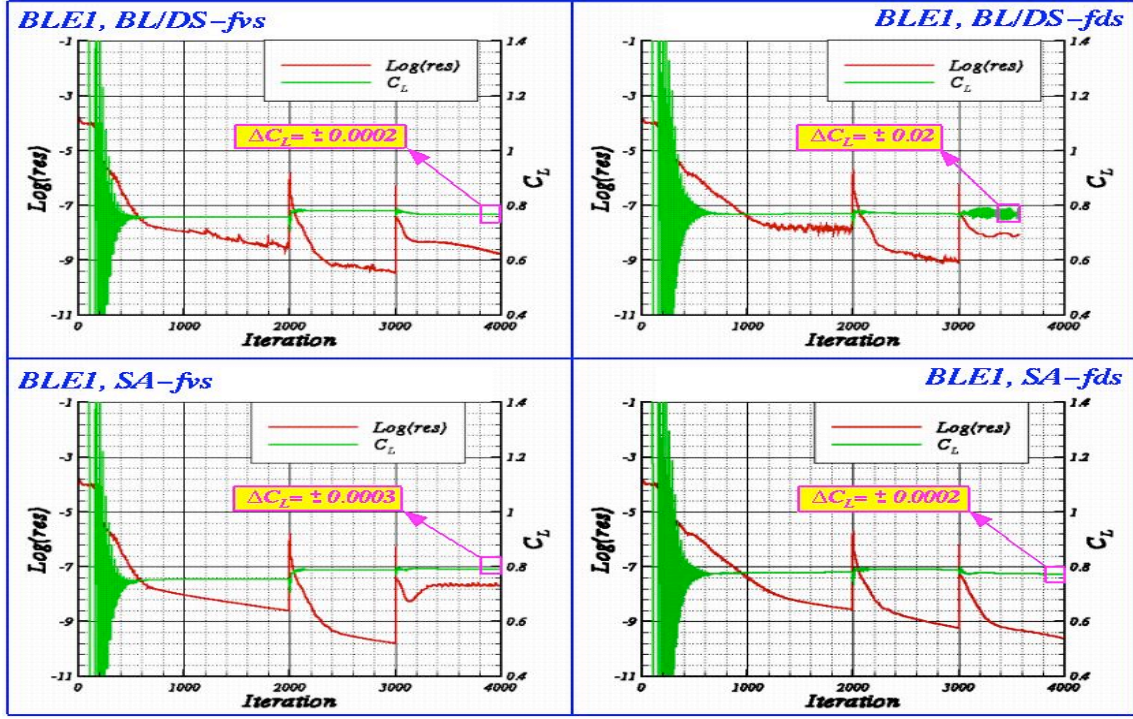


Figure 38. Turbulence model and flux splitting effects on the BLE solution convergence history at $\alpha=20.4^\circ$, $M_\infty=0.40$, $R_{\bar{c}}=6 \times 10^6$.

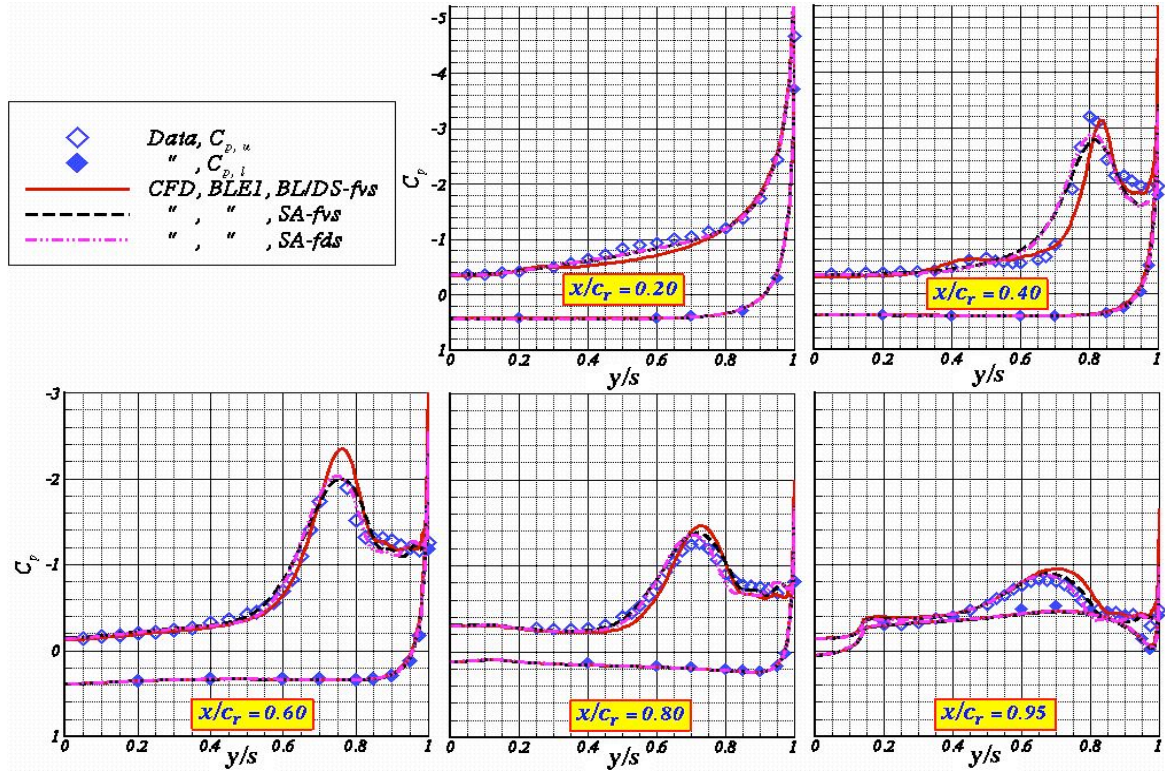


Figure 39. Turbulence model and flux splitting effects on the BLE computed C_p and correlation with data at $\alpha=20.4^\circ$, $M_\infty=0.40$, $R_{\bar{c}}=6 \times 10^6$.

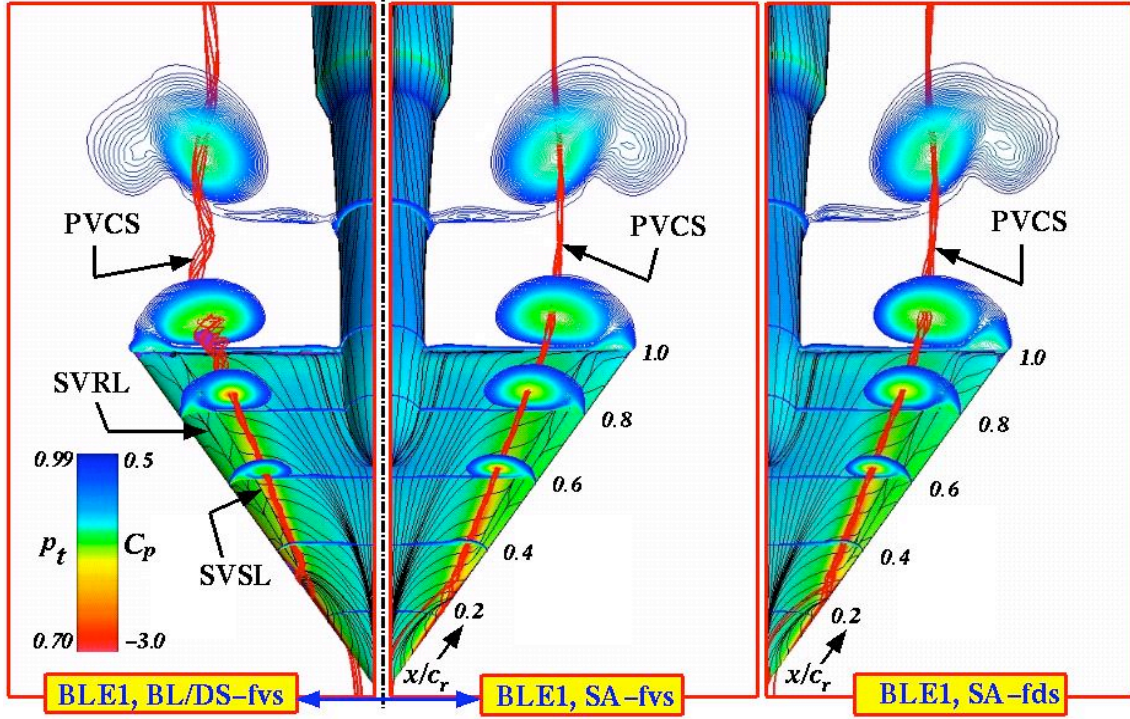


Figure 40. Effects of turbulence model and flux splitting on computed flow features using the BLE1 grid at $\alpha=20.4^\circ$, $M_\infty=0.40$, $R_c=6 \times 10^6$.

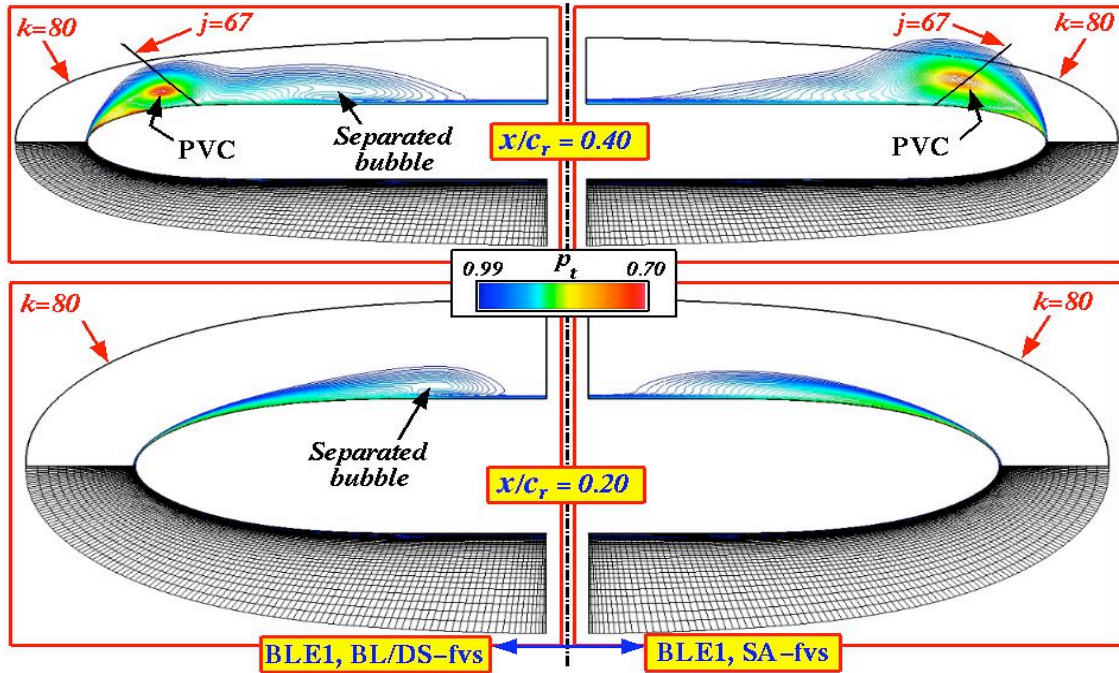


Figure 41. Effects of turbulence model on the computed wing apex flow field at $\alpha=20.4^\circ$, $M_\infty=0.40$, $R_c=6 \times 10^6$.

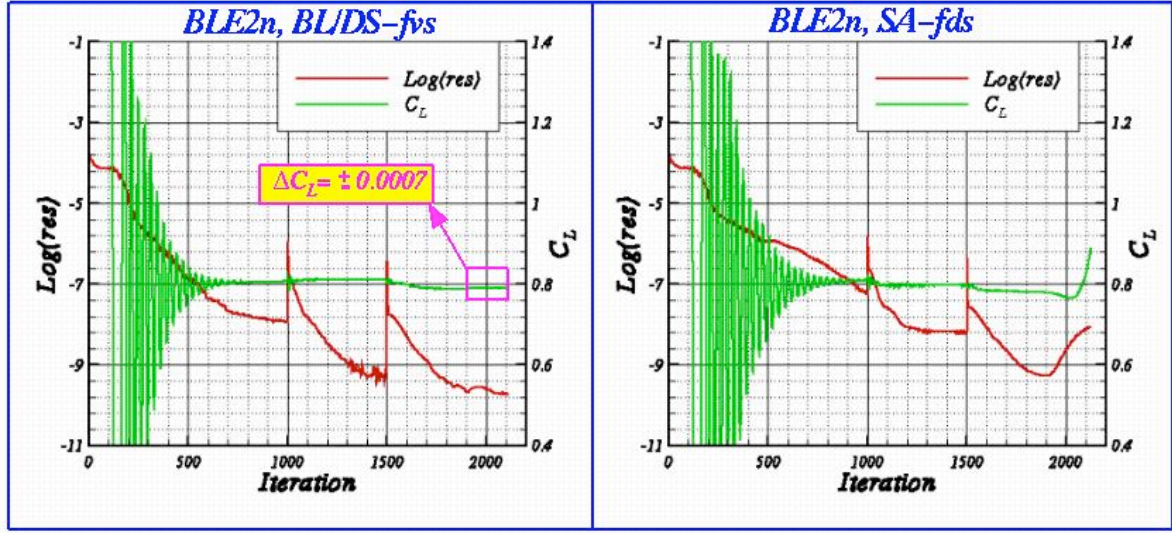


Figure 42. Solution convergence history for the computations using the BLE2n grid at $\alpha=20.4^\circ$, $M_\infty=0.40$, $R_\infty=6 \times 10^6$.

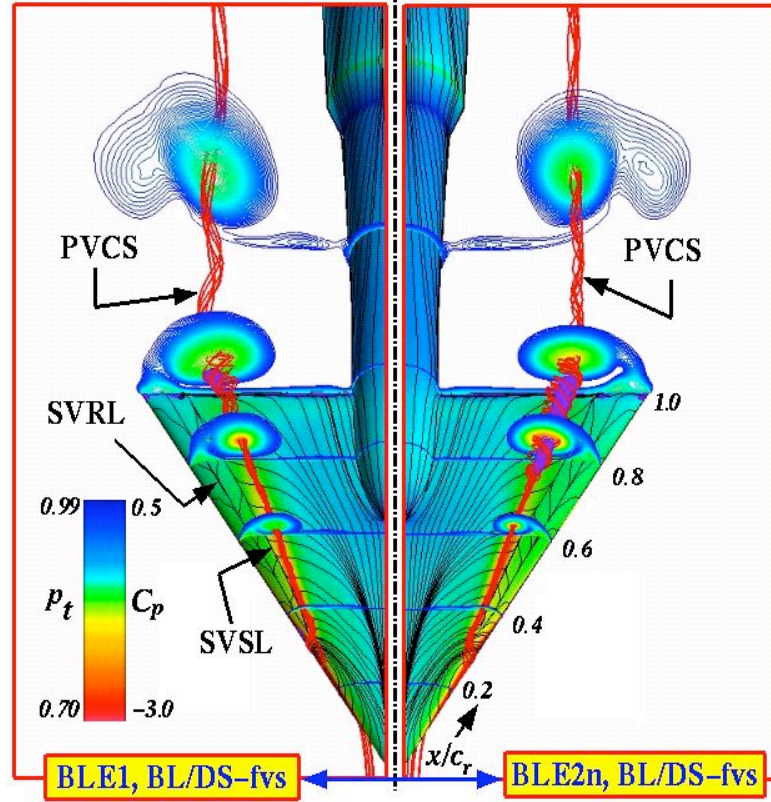


Figure 43. Effects of grid refinement on the BLE computed flow features at $\alpha=20.4^\circ$, $M_\infty=0.40$, $R_\infty=6 \times 10^6$.

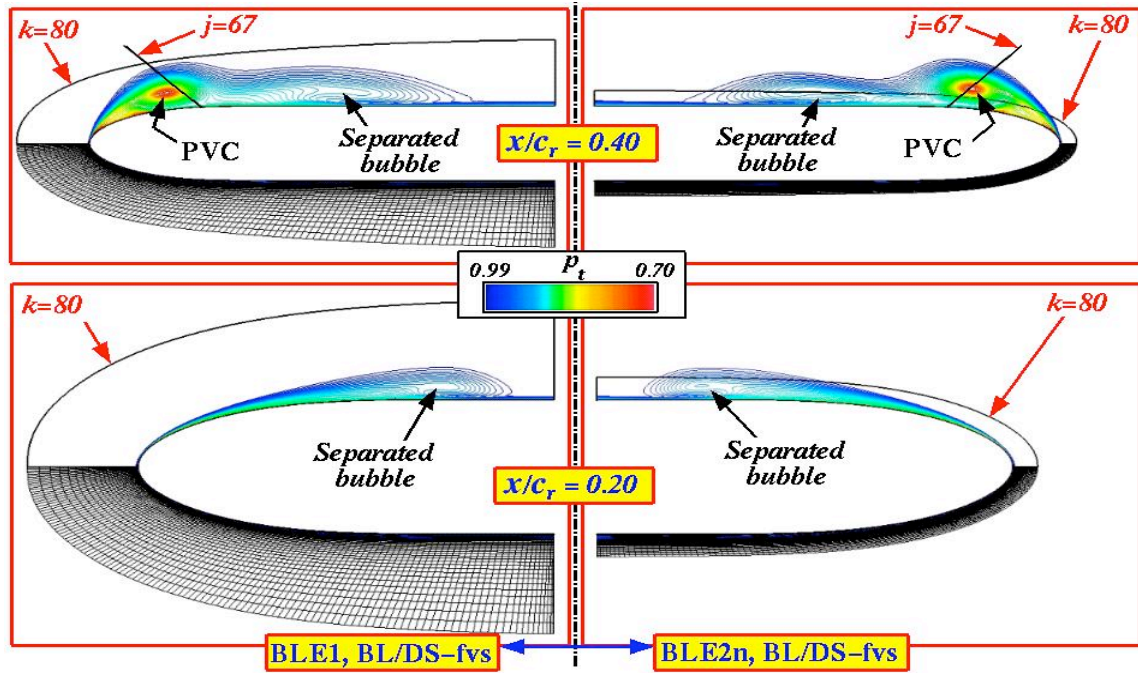


Figure 44. Effects of grid refinement on the computed wing apex flow field at $\alpha=20.4^\circ$, $M_\infty=0.40$, $R_\infty=6 \times 10^6$.

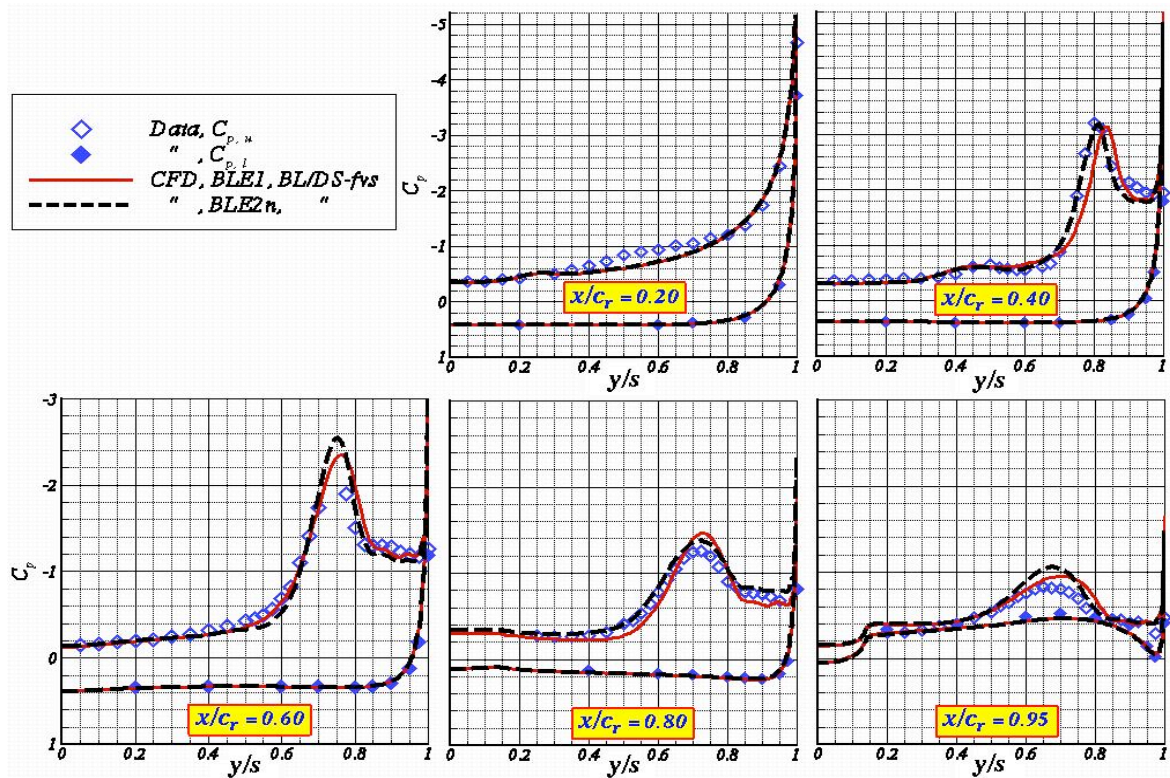


Figure 45. Effects of grid refinement on the BLE computed surface C_p at $\alpha=20.4^\circ$, $M_\infty=0.40$, $R_\infty=6 \times 10^6$.

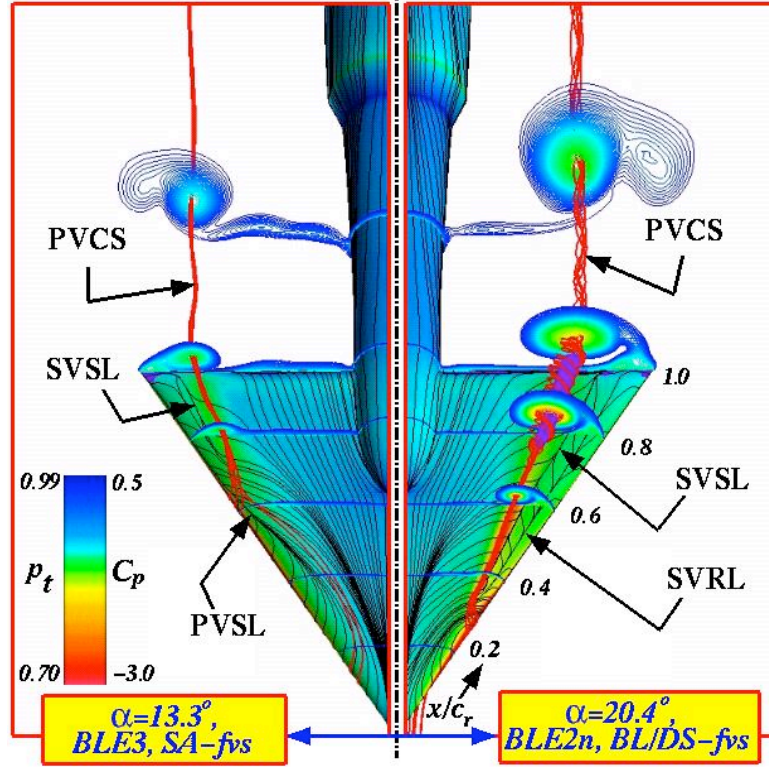


Figure 46. Effect of angle-of-attack on the BLE computed flow features at $M_\infty=0.40$, $R_c=6 \times 10^6$.

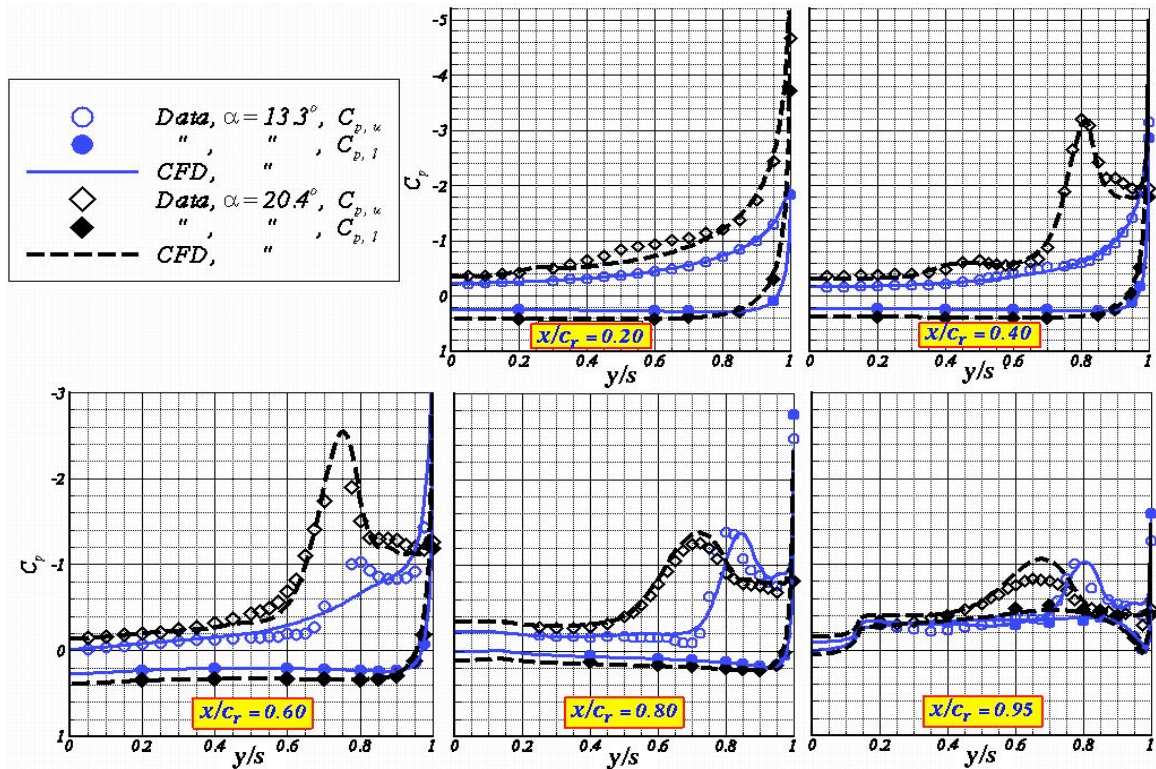


Figure 47. Effect of angle-of-attack on the BLE computed C_p and correlation with data at $M_\infty=0.40$, $R_c=6 \times 10^6$.

| REPORT DOCUMENTATION PAGE | | | | | Form Approved OMB No. 0704-0188 | |
|--|-------------|----------------------|-------------------------------|--|--|--|
| <p>The public reporting burden for this collection of information is estimated to average 1 hour per response, including the time for reviewing instructions, searching existing data sources, gathering and maintaining the data needed, and completing and reviewing the collection of information. Send comments regarding this burden estimate or any other aspect of this collection of information, including suggestions for reducing this burden, to Department of Defense, Washington Headquarters Services, Directorate for Information Operations and Reports (0704-0188), 1215 Jefferson Davis Highway, Suite 1204, Arlington, VA 22202-4302. Respondents should be aware that notwithstanding any other provision of law, no person shall be subject to any penalty for failing to comply with a collection of information if it does not display a currently valid OMB control number.</p> <p>PLEASE DO NOT RETURN YOUR FORM TO THE ABOVE ADDRESS.</p> | | | | | | |
| 1. REPORT DATE (DD-MM-YYYY) | | 2. REPORT TYPE | | | 3. DATES COVERED (From - To) | |
| 01- 07 - 2005 | | Technical Memorandum | | | | |
| 4. TITLE AND SUBTITLE Turbulent Vortex-Flow Simulation Over a 65° Sharp and Blunt Leading-Edge Delta Wing at Subsonic Speeds | | | | 5a. CONTRACT NUMBER | | |
| | | | | 5b. GRANT NUMBER | | |
| | | | | 5c. PROGRAM ELEMENT NUMBER | | |
| 6. AUTHOR(S) Ghaffari, Farhad | | | | 5d. PROJECT NUMBER | | |
| | | | | 5e. TASK NUMBER | | |
| | | | | 5f. WORK UNIT NUMBER 23-762-45-UG | | |
| 7. PERFORMING ORGANIZATION NAME(S) AND ADDRESS(ES) NASA Langley Research Center Hampton, VA 23681-2199 | | | | 8. PERFORMING ORGANIZATION REPORT NUMBER L-19140 | | |
| 9. SPONSORING/MONITORING AGENCY NAME(S) AND ADDRESS(ES) National Aeronautics and Space Administration Washington, DC 20546-0001 | | | | 10. SPONSOR/MONITOR'S ACRONYM(S) NASA | | |
| | | | | 11. SPONSOR/MONITOR'S REPORT NUMBER(S) NASA/TM-2005-213781 | | |
| 12. DISTRIBUTION/AVAILABILITY STATEMENT Unclassified - Unlimited Subject Category 02 Availability: NASA CASI (301) 621-0390 | | | | | | |
| 13. SUPPLEMENTARY NOTES An electronic version can be found at http://ntrs.nasa.gov | | | | | | |
| 14. ABSTRACT Turbulent thin-layer, Reynolds-Averaged Navier-Stokes solutions, based on a multi-block structured grid, are presented for a 65° delta wing having either a sharp leading edge (SLE) or blunt leading edge (BLE) geometry. The primary objective of the study is to assess the prediction capability of the method for simulating the leading-edge flow separation and the ensuing vortex flow characteristics. Computational results are obtained for two angles of attack of approximately 13° and 20°, at free-stream Mach number of 0.40 and Reynolds number of 6 million based on the wing mean aerodynamic chord. The effects of two turbulence models of Baldwin-Lomax with Degani-Schiff (BL/DS) and the Spalart-Allmaras (SA) on the numerical results are also discussed. The computations also explore the effects of two numerical flux-splitting schemes, i.e., flux difference splitting (fds) and flux vector splitting (fvs), on the solution development and convergence characteristics. The resulting trends in solution sensitivity to grid resolution for the selected leading-edge geometries, angles of attack, turbulence models and flux splitting schemes are also presented. The validity of the numerical results is evaluated against a unique set of experimental wind-tunnel data that was obtained in the National Transonic Facility at the NASA Langley Research Center. | | | | | | |
| 15. SUBJECT TERMS Delta wing, Flow separation, Vortex flows, Turbulent flow, Computational fluid dynamics, Navier-Stokes formulations, Structured grid | | | | | | |
| 16. SECURITY CLASSIFICATION OF: | | | 17. LIMITATION OF ABSTRACT | 18. NUMBER OF PAGES | 19a. NAME OF RESPONSIBLE PERSON | |
| a. REPORT | b. ABSTRACT | c. THIS PAGE | | | STI Help Desk (email: help@sti.nasa.gov) | |
| U | U | U | UU | 47 | 19b. TELEPHONE NUMBER (Include area code) (301) 621-0390 | |